Modeling the impact of granular embedding media, and pulling versus pushing cells on growing cell clones

Dirk Drasdo, Stefan Hoehme

Modeling the impact of granular embedding media, and pulling versus pushing cells on growing cell clones

2012 New J. Phys. 14 055025

(http://iopscience.iop.org/1367-2630/14/5/055025)

New Journal of Physics
The open-access journal for physics

Modeling the impact of granular embedding media, and pulling versus pushing cells on growing cell clones

Dirk Drasdo[1,2] **and Stefan Hoehme**[2]

[1] Institut National de Recherche en Informatique et en Automatique (INRIA), Unit Rocquencourt BP 105, 78153 Le Chesnay Cedex, France
[2] Interdisciplinary Centre for Bioinformatics, University of Leipzig, Leipzig, Germany
E-mail: dirk.drasdo@inria.fr and hoehme@uni-leipzig.de

New Journal of Physics **14** (2012) 055025 (37pp)
Received 4 October 2011
Published 31 May 2012
Online at http://www.njp.org/
doi:10.1088/1367-2630/14/5/055025

Abstract. In this paper, we explore how potential biomechanical influences on cell cycle entrance and cell migration affect the growth dynamics of cell populations. We consider cell populations growing in free, granular and tissue-like environments using a mathematical single-cell-based model. In a free environment we study the effect of pushing movements triggered by proliferation versus active pulling movements of cells stretching cell–cell contacts on the multi-cellular kinetics and the cell population morphotype. By growing cell clones embedded in agarose gel or cells of another type, one can mimic aspects of embedding tissues. We perform simulation studies of cell clones expanding in an environment of granular objects and of chemically inert cells. In certain parameter ranges, we find the formation of invasive fingers reminiscent of viscous fingering. Since the simulation studies are highly computation-time consuming, we mainly study one-cell-thick monolayers and show that for selected parameter settings the results also hold for multi-cellular spheroids. Finally, we compare our model to the experimentally observed growth dynamics of multi-cellular spheroids in agarose gel.

S Online supplementary data available from stacks.iop.org/NJP/14/055025/mmedia

Contents

1. Introduction

Most *in vivo* tumors expand into the surrounding tissue. To do so, a growing tumor must overcome mechanical barriers by either exerting mechanical stress on the host tissue (the tumor micro-environment) or secreting matrix-degrading enzymes that modify the local environment by cutting fibers such that the macroscopic mechanical resistance is lowered.

Biomechanically induced interactions are increasingly discovered to play an important role in the growth control of tissues and tumors [1–17]. Biomechanical interactions can serve as morphogenetic regulators [3] and permit cells to compare and adjust their growth rate to surrounding cells [5], help cells to choose their orientation according to their environment [6] or to adjust their growth rate to a local geometric property such as tissue curvature; this has led to the conjecture that sometimes functions follow form [7]. Morphogenetic strain rates, cell shape change and intercalation have been demonstrated to be interlinked [18].

Tumors have been observed to grow slower when their embedding medium is stiffer, and their shape may reflect the geometrical constraints of their environment [1, 14]. Chaplain *et al* [19] studied this situation in a multi-scale, multi-phase model considering tumor cells, the extracellular matrix (ECM) and the host tissue including molecular factors controlling the growth. Momentum balance was mimicked by an approach of the Darcy type, hence assuming the tumor behaves as a porous medium. They find an exponential growth for small tumors saturating at large stress. Helmlinger *et al* [1] showed the influence of the biomechanical properties of the tumor micro-environment by growing tumor spheroids embedded in agarose gels of different levels of concentration and thus rigidity. Regardless of the host species and the tissue of origin, increased mechanical stress led to significantly decreased maximal tumor spheroid sizes, which for example in human colon carcinoma decreased from a diameter of 400 μm (in 0.5% agarose) to 50 μm (in more rigid 1% agarose). Chen *et al* [20] studied the saturation of growth within a multi-phase model of a growing tumor in external poroelastic material in spherical coordinates to explain the Helmlinger experiment. The tumor was modelled as a two-phase solid–liquid material similar to a porous material where the volume fraction of

the interstitial liquid was assumed to decrease upon compression of the tumor. They found saturation after a certain time, as it was observed in the experiments and linear growth if the poroelastic gel was removed. More recently, another group demonstrated that also the shape of tumor spheroids is dictated by the shape of the solid stress field by using agarose gels and co-embedding fluorescent micro-beads [14]. Further analysis revealed that one reason for this observation was suppression of proliferation and induction of apoptosis in regions of high mechanical stress. A number of hypotheses have been proposed on the question of how and to what extent the physical interaction of tumor and host tissue influences tumor morphology and growth kinetics during cancerogenesis [21, 22]. Nevertheless, many aspects of these complex interactions remain to be experimentally elucidated [23].

Comparisons of experiments with mathematical models have shown that the increase of the cell population diameter as well as of the cell proliferation pattern, in both growing monolayers [24, 25] and growing multi-cellular spheroids [24–27], could largely be explained by a biomechanical form of contact inhibition, controlled by a force threshold, a pressure threshold or a deformation threshold, above which cells become quiescent. For example, a careful analysis of EMT6/Ro multi-cellular spheroids revealed that the size of a multi-cellular spheroid is almost unaffected even when the external glucose concentration is varied by a factor of 20 from 0.8 to 16.5 mM, while at the same time the cell population sizes varied significantly. The glucose medium concentration only affected the size of the necrotic core, but not the tumor size. Even the growth kinetics of well-vascularized xenografts of human NIH3T3 cells subcutaneously injected into mice could be explained by the same form of biomechanical growth control [28].

These examples clearly indicate that biomechanical effects have a potentially important role in growth and form.

However, unlike physical particles, biological cells have the capability to change their physical properties by intracellular control processes and thereby modify their phenotype. A prominent example is the epithelial–mesenchymal transition (EMT; see, e.g. [29]) in cancer where the tissue phenotype changes from an epithelium-type phenotype to a mesenchymal phenotype by active intracellular regulation facilitating cell detachment [30–32]. Another example is that cells are able to enter blood vessels by a process called intravasation involving cancer-cell-induced src activation, leading to the degradation of contacts among endothelial cells, and thereby decrease the mechanical resistance of the blood vessel walls against cancer cell invasion [33]. Cell birth and death may facilitate cell movement in tissues which on short time scales appear as elastic material [16].

These examples suggest that there is a complex interplay of mechanical and active regulative components during different stages of tumor growth, development and invasion. To find out the contributions of different active versus passive components it is important to examine how far the cancer phenotype can be explained by physical effects alone. Otherwise, morphotypes may be erroneously attributed to active regulatory behavior of cancer cells. Invasive fingers, for example, can also be triggered purely by physical effects as known from viscous fingering [34] or other instabilities known from non-equilibrium physics (see, e.g. [35, 36]). Examples are the Mullins–Sekerka instability of a growing crystal in a supercooled melt driven by undercooling at the solid–liquid interface (see, e.g. [37, 38]), and an elasticity-driven growth instability as a consequence of an applied stress [39], a buckling instability driven by the competition of cell proliferation and stabilizing effects such as bending or shear (see, e.g. [8, 40–42]), or an undulation stability as it may occur at the epithelial stromal

interface again driven by cell proliferation ([43]; see also text below). Different morphotypes have observed bacterial growth which could be explained by different types of instabilities [44].

In this paper, we explore how far physical properties of the embedding medium of a growing cell clone affect the emerging spatial–temporal growth pattern. For this purpose we consider two situations, namely a growing clone of cells in a granular medium and a growing clone in an environment of inert cells. Within our model the main difference between the two situations is that for cells we assume an active component of the movement, the cell micro-motility, whereas for the granular objects we do not. We do not take into account the active regulation mechanisms for cells as reported in, for example [30, 33]. We mimic each biological cell individually within the framework of 'agent-based models'. Our model is based on an earlier approach where cells have been mimicked as adhesive homogeneous isotropic elastic objects capable of active migration, growth and division of particles. This model has permitted us to explain the growth pattern of monolayers and multi-cellular spheroids [24–27] and predicted a subsequently validated order principle in the regenerating liver [45].

We consider a growing monolayer as the reference situation. Recent experiments in [46] suggest, for expanding monolayers of MDCK (Madin–Darby canine kidney) cells, an active migration into the direction of the outwards-pointing normal of the cell population border. The cell density as well as the cell traction has been reported to increase from the border to the middle of the monolayer. This suggests a pulling type of movement—perhaps in combination with an increasing contraction of the cell projection area from the border to the center [47]. In a recent paper [45], we could show that active directed cell movement is necessary for explaining the regeneration of a CCl_4-induced tissue lesion in mouse liver. Passive movement triggered by cell proliferation alone was insufficient. However, in both cases the cell populations were not constrained by the strong resistance of other cells or a capsule.

In contrast, in liver regeneration after partial hepatectomy, the growth of a cell population must occur against the resistance of a capsule enclosing the liver lobes. Hence, growth in such an environment must occur against mechanical resistance.

The above-reported observations [45, 46] suggest that both types of movement may exist: (i) pushing-type fronts if cell division leads to local mechanical stress pushing neighbor cells into the direction of minimal mechanical compression. (ii) Pulling-type movement may be triggered by the emergence of a border, resulting in active cell migration into the free zone. For this reason we compare the effect of a biased micro-motility with the existence of an un-biased micro-motility. In [24–27] we had only considered the case of an un-biased (i.e. uniformly distributed) micro-motility.

We first consider growing monolayers with a free border and briefly discuss cell movement triggered either by cell division ('pushing-type movement') or by an active outwards 'pulling-type movement' of cells.

For growing clones embedded in tissues or tissue-like media, a free cell population border does not exist. Instead, an external medium exerts a pressure on the expanding clone resembling a carcinoma located in an organ (such as e.g. a liver carcinoma) or a population of hepatocytes enclosed by a capsule rather than a tumor expanding in free space or in a soft tissue environment. In such a situation a pulling-like movement of the tumor cells seems unlikely to occur prior to the EMT.

So, in summary, the main purpose of this paper is to explore the growth and invasion pattern of biological cells in a minimum model mimicking cells as homogeneous isotropic elastic, sticky particles capable of self-reproduction and migration.

In section 2, we present the basic model and its variants used in this paper.

Then we consider pushing- and pulling-type expansion of monolayers in a liquid environment. We then study monolayers expanding in external media of different properties, namely granular objects and cells of different types. We mainly consider simulations in two dimensions noting, however, that in three dimensions the results should be equivalent as long as glucose or oxygen do not become limiting, which seems to hold over a wide range of glucose and oxygen concentrations [24]. We demonstrate this by simulations of multi-cellular spheroids embedded in granular objects in three dimensions.

2. The model

We model each individual cell by an isotropic, elastic and adhesive object. The model cells are capable of active migration, growth and division and are defined by cell-kinetic, biophysical and cell-biological parameters that can be experimentally measured. Model cells interact with each other, with other cells and with the underlying substrate.

2.1. Cell shape and cell–cell interaction

In particular, epithelial-derived tumor cells and epithelial cells may reveal a largely spherical shape in isolation as shown in [45] (see supporting information in that reference). In culture at high cell densities they adopt a polygonal shape.

When a cell gets into touch with another cell it can form an adhesive cell–cell contact. With decreasing distance between cells (e.g. upon compression), the contact area between them, and with it the number of adhesive bonds, increases, resulting in increasing attractive interaction. On the other hand, if cells in isolation are spherical, an increasing contact area is accompanied by an increasing deformation, which results in a repulsive interaction. Hence, the preferred distance of a pair of interacting cells is where adhesive and repulsive forces balance. If adhering cells are pulled from each other they reveal a hysteresis effect: they elongate and stick beyond the distance at which they had come into contact. At the rupture point they still have a finite interaction area. These observations had led the authors of [24] to approximate the interaction forces between cells by the Johnson–Kendall–Roberts (JKR) model. The same model has independently been shown in [48] to apply to pairwise interacting S180 cells using micro-pipette experiments. The JKR model mimics the force between a pair of interacting sticky homogeneous isotropic spherical objects. It directly includes adhesion and relates the contact area to the elastic material properties and the adhesion strength and therefore gives in the limit studied in [48] a proper quantitative description.

The JKR force $F_{ij}^{\mathrm{JKR}} = |\underline{F}_{ij}^{\mathrm{JKR}}(d_{ij})|$, where d_{ij} is the distance between the centers of two interacting spheres i and j that is calculated from two implicit equations [49]:

$$\delta = \frac{a^2}{\tilde{R}} - \sqrt{\frac{2\pi\hat{\gamma}a}{\tilde{E}_{ij}}}, \tag{1}$$

$$a^3 = \frac{3\tilde{R}}{4\tilde{E}_{ij}}\left[F_{ij}^{\mathrm{JKR}} + 3\pi\hat{\gamma}\tilde{R} + \sqrt{6\pi\hat{\gamma}\tilde{R}F_{ij}^{\mathrm{JKR}} + (3\pi\hat{\gamma}\tilde{R})^2}\right], \tag{2}$$

where a is the contact radius. The effective radius $\tilde{R}$ is defined by $\tilde{R}^{-1} = R_i^{-1} + R_j^{-1}$, where R_i is the radius of cell i. $d_{ij} = R_i + R_j - \delta$ is the distance between the centers of model cell

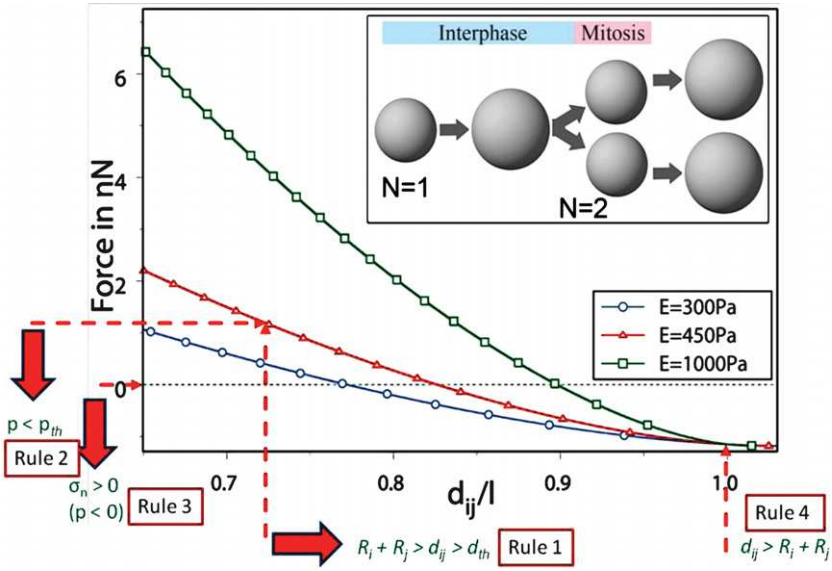

Figure 1. The force F_{ij} as a function of the distance d_{ij} for two interacting spheroidal cells i, j according to the JKR model for three different elastic moduli, $E_i = E_j = 300$, 450 and 1000 Pa. The dashed red lines illustrate different cell-cycle entrance control conditions that we tested. Rule 1 assumes a compression threshold, assuming that a cell i can only enter the cell cycle if its distance d_{ij} to its neighbor cell j remains larger than d_{th}. This rule introduced in [24] is not considered here. Rule 2 assumes that cells can only enter the cell cycle if the pressure-like measure $p_i = \sum_j F_{ij}/A_{ij}$ (A_{ij} is the contact area) is below a threshold $p_{\mathrm{th}} > 0$ (the sum is over all neighbors of i; for details see text). Rule 3 assumes that only cells that experience a negative pressure are able to enter the cell cycle. Rule 4 assumes that only if the cell–cell contact to at least one neighbor cell is stretched is it able to enter the cell cycle. Inset: cell division in the program. Cells double their volume in interphase and deform into a dumbbell in mitosis. ($\nu_i = \nu_j = 0.4$, $\varsigma_m = 10^{15}\,\mathrm{m}^{-2}$.)

i and cell j, where $\delta = \delta_i + \delta_j$ is the sum of the deformations of each cell (upon compression it is the overlap of the two spheres) along the axis linking the centers of these cells. $\tilde{E}_{ij}$ is the composite Young's modulus defined by $\tilde{E}_{ij}^{-1} = (1-\nu_i^2)E_i^{-1} + (1-\nu_j^2)E_j^{-1}$. We approximate $\hat{\gamma} \approx \varsigma_m W_s$. ϱ_m is the density of cell–cell adhesion molecules in the cell membrane, W_s the energy of a single bond. If the density of cell adhesion molecules would differ in two cell i and j in contact, then $\varrho_m = \min(\varrho_i, \varrho_j)$. In our simulations we assume the same cell adhesion molecule density for each cell. Equation (2) has to be solved implicitly to obtain $a(F_{ij}^{\mathrm{JKR}})$. The value of a is then inserted into equation (1) to give $\delta(a)$, $d_{ij} = R_i + R_j - \delta$, $d_{ij}(a)$. $F_{ij}^{\mathrm{JKR}}(d_{ij})$ can be obtained by plotting $F_{ij}^{\mathrm{JKR}}(d_{ij})$ versus d_{ij} (figure 1) as the equations (1) and (2) are not amenable to an explicit solution if $\hat{\gamma} > 0$. We fitted the resulting plot by a polynomial of degree three and used this polynomial in the simulations. In this way, were able to avoid a prolongation of the simulation times, which would occur if the JKR model equations were solved numerically during the simulation runs with the multi-cellular growth model, and to keep the advantages of

the JKR force outlined above:

$$F_{ij}^{\mathrm{JKR}}(d_{ij}) \approx a_3(d_{ij})^3 + a_2(d_{ij})^2 + a_1(d_{ij}) + a_0. \tag{3}$$

The force vector denoting the force of cell j on cell i results from

$$\underline{F}_{ij} = F_{ij}^{\mathrm{JKR}}(d_{ij}) \frac{\underline{r}_i - \underline{r}_j}{|\underline{r}_i - \underline{r}_j|}.$$

Certainly, although the JKR-force model seems to be a plausible approximation for the interaction between cells, it neglects inhomogeneities of the cell material, deviations of the cell shape from a spherical shape prior to deformation and plastic deformations that are expected to occur on longer time scales as a consequence of re-organization processes of the cytoskeleton. Moreover, the force calculated by the JKR model is a two-body force and neglects forces that may emerge from multi-body interactions. However, in [26] we have shown that multi-cellular growth phenomena in liquid suspension or monoclonal monolayers show only moderate differences if the interaction force model is varied, for example, by using an extended Hertz model or a linear spring-like interaction force between cells. From this we would not expect any qualitative impact from replacing the JKR-force model by a more detailed description of interaction forces even though we consider it as an important challenge in the future, as far as quantitative experiments permit a more detailed measurement of the forces to allow increasingly quantitative model predictions. On the other hand, we consider it useful to take the JKR force instead of a cruder interaction force, as it is parameterized in measurable quantities and is expected to be correct for sufficiently fast deformations.

We here consider perfect one-cell-thick monolayers. They can experimentally be realized in two ways. As we have shown earlier [25], cells seeded on a flat substrate do not detach from the substrate if their growth is contact inhibited and if at the same time the cell-substrate forces are sufficiently strong to ensure that the cells enter the cell cycle rest (G_0-) phase before they would detach from the substrate. Therefore, contact-inhibited cell lines with sufficiently strong substrate adhesion would form a one-cell-thick monolayer. Another experimental possibility to ensure the formation of a perfect one-cell-thick monolayer might be to constrain the monolayer from above so that cells cannot leave the one-cell-thick layer configuration even if they are not contact-inhibited. We use the JKR force also for the adhesion between cells and the underlying substrate.

2.2. Cells and the enclosing medium

The expanding cells can grow and divide as explained below. We consider two types of environmental objects: non-dividing cells or inert granular objects. We label the cells of the expanding clone 'A' and the enclosing objects 'B'. Below we refer to the cells of the expanding clone as 'A-cells' and to objects (cells or granular objects) of the enclosing medium as 'B-objects'.

2.3. Cell growth and division

During G_1-, S- and G_2-phase we assume that a cell increases its volume by increasing the radius R in small steps $\triangle R \ll R$ until it has doubled its initial 'intrinsic' volume to $V_{\mathrm{DIV}} = 2V_{\mathrm{INIT}}$, where V_{INIT} is its volume immediately after cell division (figure 1). Here, the intrinsic volume V_i of a model cell i is approximated by $V_i(R_i) = 4\pi R_i^3/3$. If $V_i = V_{\mathrm{DIV}}$ (hence $R_{\mathrm{DIV}} \approx 1.26 \cdot R$)

the model cell i deforms into a dumb-bell at constant volume. Then it divides into two daughter cells of radius R. We assume that a cell i in G_1 switches into a rest phase G_0 if the measure p_i^{tot}, defined by

$$p_i^{\mathrm{tot}} = \sum_{j\,NN\,i} \left(\frac{\underline{F}_{ij}^{\mathrm{AA}}}{A_{ij}} \frac{\underline{r}_i - \underline{r}_j}{|\underline{r}_i - \underline{r}_j|} \right) + \sum_{j\,NN\,i} \left(\frac{\underline{F}_{ij}^{\mathrm{AB}}}{A_{ij}} \frac{\underline{r}_i - \underline{r}_j}{|\underline{r}_i - \underline{r}_j|} \right) + \frac{\underline{F}_{i\mathrm{S}}^{\mathrm{AS}}}{A_{i\mathrm{S}}} \frac{\underline{r}_i - \underline{r}_j}{|\underline{r}_i - \underline{r}_j|},$$

overcomes a threshold value p_0. p_i^{tot} is a pressure-like measure (hereinafter referred to as 'pressure').

Here, $\underline{F}_{ij}^{\mathrm{AA}}$ is the JKR force between A-cell i and a neighbor j of type A, $\underline{F}_{ij}^{\mathrm{AB}}$ is that between A-cell i and a neighbor j of type B, $\underline{F}_{i\mathrm{S}}^{\mathrm{AS}}$ is that between A-cell i and the flat substrate, and A_{ij} are the corresponding contact areas calculated with the JKR model. In the first sum of the above relation, j runs over the nearest neighbors of type A, and in the second sum, it runs over the nearest neighbors of type B. The pressure is calculated directly after the division of a cell. If $p_i^{\mathrm{tot}} \leqslant p_0$, then the cell i enters the cell cycle and passes through the whole cell cycle again. If the forces on cell i were isotropically distributed, acting uniformly on the whole cell surface, and if the adhesion strength were zero, the measure is identical to the definition of hydrostatic pressure on the cell.

The orientation of cell division in the monolayer simulations is assumed to be random uniformly distributed parallel to the two-dimensional (2D) substrate. During the mitosis phase we assume that cells adopt for a short time period a dumb-bell shape. Forces on cells at this stage can lead to a torque. The orientation can change as a consequence of the torque which we take into account by orientation changes. For simplicity we modeled these by energy minimization (the Metropolis algorithm) instead of numerically integrating equations for the torques. Energy minimization provides an alternative to a forced-based single-cell dynamics [26]. Within each time interval Δt for each cell a rotation trial around three space-fixed axes by angles $\delta\beta_i$ with $i = 1, 2, 3$, $\delta\beta_i \in [0, \delta\beta_{\max})$, with $\delta\beta_{\max} \ll \pi/2$ was performed, using the algorithm of Barker and Watts as explained in [26]. The probability P_{Rot} that the rotation trial is accepted was calculated by $P_{\mathrm{Rot}} = \min(1, \mathrm{e}^{(-\Delta V/F_{\mathrm{T}})})$ where $\Delta V = V(t+\Delta t) - V(t)$. $V(t+\Delta t) = \sum_{i<j}^{N} V_{ij}(t+\Delta t)$ is the total potential energy after the orientation change and $V(t)$ the total potential energy before the orientation change. F_T is a reference energy [24]. The energy and force can directly be linked by $\underline{F}_{ij} = -\partial V_{ij}/\partial \underline{r}_i$. The Metropolis algorithm ensures that orientation changes that lead to a decrease of the energy of the multi-cellular configuration are always accepted, while those which lead to an energy increase are only accepted with probability $\mathrm{e}^{-\Delta V/F_{\mathrm{T}}}$. For spherical cells we do not consider orientation changes since they do not change the total energy of the multi-cellular configuration. For the monolayers the cell-substrate forces were assumed to be strong enough to prevent cells from moving out of the layer.

2.4. Cell migration

First, the modeling framework for monolayers is developed, where cells can crawl on a 2D substrate. After this, we discuss the difference between monolayers and multi-cellular spheroids, which are 3D cell aggregates.

Monolayers. In the absence of chemotactic signals, isolated cells in suspension or culture medium have been observed to perform an active random-walk-like movement in monolayers [50, 51]. We assume that the random component of the active cell motion, the

cell micro-motility, can be characterized by the cell diffusion constant D of isolated randomly moving cells. We used $D_0 \approx 10^{-12}\,\mathrm{cm}^2\,\mathrm{s}^{-1}$ as the reference value. More motile cells are characterized by a larger D. In our model, D is also used to quantify the micro-motility of cells in contact with other cells.

While in mechanical contact with other cells, proliferating cells exert a pressure on their neighbors. The neighboring cells try to escape this pressure by moving against the friction caused by the other neighbor cells and extracellular material, for example ECM [52]. The movement could be partly passive, due to pushing, and partly active [9, 46], if cells migrate into the direction in which they escape the mechanical (or morphogen) stimulus. We simulate cell migration as a friction-dominated over-damped motion with a stochastic contribution by a stochastic equation of motion for each cell [26, 45, 53]. Schienbein *et al* [50] have demonstrated that the migration of an ensemble of isolated cells in culture subject to an external force can be mimicked by a Fokker–Planck equation for the single-particle distribution function having a drift and a diffusion term.

Dickinson and Tranquillo [54, 55] have developed equations of motions for different types of cell movement from cell receptor dynamics and obtained a stochastic dynamics reminiscent of the approach of [50]. More recently, in [46], in monolayers of MDCK cells a net traction of cells perpendicular to the border of the layer was observed, suggesting an active pulling-like movement to increase the spread of the monolayer. Our equation of motion tries to capture the main aspects of these observations.

The equation of motion of cell i of the expanding cell type (denoted by the superscript A) is determined by

$$\sum_s \underline{\underline{\zeta}}_{is}^{\mathrm{AS}} \underline{v}_i^{\mathrm{A}}(t) = \sum_{jNNi} \left(\underline{\underline{\zeta}}_{ij}^{\mathrm{AA}} (\underline{v}_j^{\mathrm{A}}(t) - \underline{v}_i^{\mathrm{A}}(t)) + \underline{F}_{ij}^{\mathrm{AA}} \right) + \underline{F}_i^{\mathrm{Active,A}} + \sum_{jNNi} \left(\underline{\underline{\zeta}}_{ij}^{\mathrm{AB}} (\underline{v}_j^{\mathrm{B}}(t) - \underline{v}_i^{\mathrm{A}}(t)) + \underline{F}_{ij}^{\mathrm{AB}} \right) + \underline{F}_i^{\mathrm{AS}}.$$

In this equation, $\underline{v}_i^{\mathrm{A}}(t)$ is the velocity of cell i of type A and $\underline{v}_i^{\mathrm{B}}$ is the velocity of object i of type B. $\underline{\underline{\zeta}}_{ij}^{\mathrm{AX}}$ with $\mathrm{X} = \{\mathrm{A}, \mathrm{B}, \mathrm{S}\}$ denotes the friction of cell i of type A and (i) cell j of type A (if $\mathrm{X} = \mathrm{A}$) or (ii) object j of type B (if $\mathrm{X} = \mathrm{B}$) or (iii) the substrate S (if $\mathrm{X} = \mathrm{S}$). Generally, the friction may be decomposed into a perpendicular and a parallel component, so that

$$\underline{\underline{\zeta}}_{ij}^{\mathrm{AX}} = \gamma_{\perp}^{\mathrm{AX}} (\underline{u}_{ij} \otimes \underline{u}_{ij}) + \gamma_{\parallel}^{\mathrm{AX}} (\underline{\underline{I}} - \underline{u}_{ij} \otimes \underline{u}_{ij}).$$

Here, $\underline{u}_{ij} = (\underline{r}_j - \underline{r}_i)/|\underline{r}_j - \underline{r}_i|$ with $\underline{r}_i$ denoting the center of cell i of type A (or if cell i is in mitosis and has a dumb-bell shape, the position of the closest sphere of the dumb-bell). $\underline{r}_j$ denotes the center of object $\mathrm{X} \in \{\mathrm{A}, \mathrm{B}, \mathrm{S}\}$ i.e. a cell of type A, an object of type B, or the substrate S. '$\otimes$' denotes the dyadic product. $\underline{F}_{ij}^{\mathrm{XY}}$ denotes the JKR force between cells i and j of type A ($\mathrm{X} = \mathrm{Y} = \mathrm{A}$), objects i and j of type B ($\mathrm{X} = \mathrm{Y} = \mathrm{B}$) or between cell i of type A and object j of type B ($\mathrm{X} = \mathrm{A}$, $\mathrm{Y} = \mathrm{B}$ or $\mathrm{X} = \mathrm{B}$, $\mathrm{Y} = \mathrm{A}$). $\underline{F}_i^{\mathrm{AS}}$ is the JKR-force between cell i of type A and the substrate S. The JKR-forces between cells A and the substrate and between objects B and the substrate are assumed to be large enough to prevent detachment and are not explicitly modeled here. We assume the substrate that the cell crawls on to be flat and denote it by a sphere of infinite radius. $\underline{\underline{I}}$ is the unity matrix. $(\underline{u} \otimes \underline{u})\underline{v}_i$ is the projection of $\underline{v}_i$ on $\underline{u}$. This can be immediately seen as, after

some re-writing,

$$\underline{\underline{\zeta}}_{ij}^{\mathrm{AX}}\underline{v}_i = \gamma_{\perp}^{\mathrm{AX}}(\underline{u}_{ij}\otimes\underline{u}_{ij})\underline{v}_i + \gamma_{\parallel}^{\mathrm{AX}}(\underline{\underline{I}} - \underline{u}_{ij}\otimes\underline{u}_{ij})\underline{v}_i$$
$$= \gamma_{\perp}^{\mathrm{AX}}\underline{u}_{ij}(\underline{u}_{ij}\underline{v}_i) + \gamma_{\parallel}^{\mathrm{AX}}(\underline{\underline{I}}\,\underline{v}_i - \underline{u}_{ij}(\underline{u}_{ij}\underline{v}_i)).$$

If, for example, X = S, then $\underline{u}_{ik}$ is the unit vector of the line connecting the center of the sphere of infinite radius representing the substrate $k = s$ and the center of cell i of type A. $(\underline{u}_{is}\otimes\underline{u}_{is})\underline{v}_i$ then denotes the projection of the velocity component on the connecting line, i.e. perpendicular to the substrate, and $(\underline{\underline{I}} - \underline{u}_{is}\otimes\underline{u}_{is})\underline{v}_i$ is the velocity component parallel to the substrate. Accordingly, $\gamma_{\parallel}^{\mathrm{AS}}$ denotes the tangential friction coefficient of a cell of type A with the substrate. Correspondingly, $(\underline{u}_{is}\otimes\underline{u}_{is})\underline{v}_i$ would contribute to a deformation of a sphere against inner cell friction characterized by $\gamma_{\perp}^{\mathrm{AS}}$. In general, the friction coefficients $\gamma_{\perp}^{\mathrm{XY}}$, $\gamma_{\parallel}^{\mathrm{XY}}$ may differ for cells of type A and objects of type B. We assume here that they are the same i.e. $\gamma_{\perp}^{\mathrm{AA}} = \gamma_{\perp}^{BB}$ and $\gamma_{\parallel}^{\mathrm{AA}} = \gamma_{\parallel}^{\mathrm{BB}}$. We further assume throughout this paper that $\gamma_{\perp}^{\mathrm{XY}} = 0$ and that $\gamma_{\parallel}^{\mathrm{XY}} \propto A_{ij}$ for two interacting objects i, j of type X, Y (XY = AA, AB, BB, AS or BS). As we set $\gamma_{\perp}^{\mathrm{XY}} = 0$, we in the following use the simplified notion $\gamma^{\mathrm{XY}} \equiv \gamma_{||}^{\mathrm{XY}}$. Assuming that $\gamma^{\mathrm{XY}} \propto A_{ij}$ assumes that the density of surface adhesion molecules responsible for the strength of the friction force is nearly constant. If the number of surface molecules were constant, then γ^{XY} should be independent of A_{ij}.

$\underline{F}_{ij}^{\mathrm{AA}}$ is the JKR force the cell i of type A experiences from neighbor cell j of type A, $\underline{F}_{ij}^{\mathrm{AB}}$ is the force that A-cell i experiences from a neighbor j of type B, and $\underline{F}_{ij}^{\mathrm{AS}}$ summarizes the force A-cell i experiences from the flat substrate, ECM and a possible plate or mesh preventing movements perpendicular to the substrate. In monolayers, cells are usually attached to a substrate, usually the culture plate. $\underline{F}_i^{\mathrm{active,A}}$ is then the active migration force of cell i of type A from crawling on the substrate.

The equation of motion of the external objects (denoted by the superscript B), either external medium cells or granular particles, is mimicked by

$$\sum_s \underline{\underline{\zeta}}_{is}^{\mathrm{B}}\underline{v}_i^{\mathrm{B}}(t) = \sum_{jNNi}\left(\underline{\underline{\zeta}}_{ij}^{\mathrm{BB}}\left(\underline{v}_j^{\mathrm{B}}(t) - \underline{v}_i^{\mathrm{B}}(t)\right) + \underline{F}_{ij}^{\mathrm{BB}}\right) + \underline{F}_i^{\mathrm{active,B}}$$
$$+ \sum_{jNNi}\left(\underline{\underline{\zeta}}_{ij}^{\mathrm{AB}}\left(\underline{v}_j^{\mathrm{A}}(t) - \underline{v}_i^{\mathrm{B}}(t)\right) + \underline{F}_{ij}^{\mathrm{AB}}\right) + \underline{F}_i^{\mathrm{BS}}.$$

Equivalently, $\underline{F}_{ij}^{\mathrm{BB}}$ is the JKR force B-cell i experiences from neighbor cell j of type B, and $\underline{F}_{ij}^{\mathrm{BS}}$ is the JKR force of B-cell i by the flat substrate, extracellular material and a constraining plate or mesh.

If the B-type objects are granular particles, $\underline{F}_i^{\mathrm{active,B}} = 0$. For the other cases, the active migration force of cell B is as defined below.

Beysens *et al* [56] have proposed an analogue of an 'Einstein relation', linking the cell diffusion constant with an effective temperature. Note, however, that the physics for cells and colloidal particles is very different. For cells, the effective temperature parameter is controlled by the cell surface receptor dynamics and not, as for Brownian particles, by collisions with smaller solvent particles. If the cell motion occurs on a flat substrate, then the random micro-motility is not isotropic in three dimensions but needs to be split into components parallel and perpendicular to the substrate.

For A-type cells we consider two types of micro-motility which are presented below for a one-cell-thick monolayer.

Case 1: Unbiased micro-motility. We assume that the micro-motility is isotropic within the plane of the substrate. In this case, $\underline{F}_{i;\perp}^{\mathrm{active,A}}(t) = (\underline{u}_{is}(t) \otimes \underline{u}_{is}(t))\underline{F}_i^{\mathrm{active,A}}(t)$ is the random force component perpendicular, and $\underline{F}_{i;\parallel}^{\mathrm{active,A}}(t) = (I - \underline{u}_{is}(t) \otimes \underline{u}_{is}(t))\underline{F}_i^{\mathrm{active,A}}(t)$ is the random force component parallel to the substrate. We assume the perpendicular components to be zero. For the parallel components, we assume that $\langle \underline{F}_{i;\parallel}^{\mathrm{active,A}} \rangle = 0$, $\langle \underline{F}_{i;\parallel}^{\mathrm{active,A}}(t)\underline{F}_{i;\parallel}^{\mathrm{active,A}}(t') \rangle = 4\gamma_\parallel^2 D_\parallel \delta(t - t')$ in formal analogy with colloidal particles. Moreover, the random force components of different cells as well as between different vector components of the same cell are uncorrelated. However, as discussed above the Einstein relation in the case of cells only represents a formal analogy because unlike colloidal particles cells can control their migratory activity on their own. Hence the amplitude of the force autocorrelation function generally is a function of cell internal processes or states.

Case 2: Biased micro-motility. We assume that the active migration is biased into the direction of minimum stress exerted by A-cells if no embedding medium exists. We found that this assumption was able to explain the regeneration of the necrotic zone that emerges after intoxication by CCl_4 in liver lobules [45]. Moreover, recent monolayer experiments with MDCK cells suggest that cells may actively move towards free spaces and pull other cells behind [46]. We mimic aspects of this type of micro-motility in two alternative ways:

1. By the selection of random force contributions into directions of decreasing local pressure: $\underline{F}_i^{\mathrm{active,A}} = (1 - \Theta[\underline{\nabla} p_i \underline{f}_i^{\mathrm{active,A}}])\underline{f}_i^{\mathrm{active,A}}$, where $\underline{f}_i^{\mathrm{active,A}}$ obeys the same relations as $\underline{F}_i^{\mathrm{active,A}}$ in case 1 of isotropic micro-motility in the plane of the substrate, i.e. $\langle \underline{f}_{i;\parallel}^{\mathrm{active,A}} \rangle = 0$, $\langle \underline{f}_{i;\parallel}^{\mathrm{active,A}}(t)\underline{f}_{i;\parallel}^{\mathrm{active,A}}(t') \rangle = 4(\gamma_\parallel^{\mathrm{AS}})^2 D_\parallel \delta(t - t')$, and $\underline{f}_{i;\perp}^{\mathrm{active,A}} = 0$. Here, $\Theta(x)$ is the Heaviside function which is one if $x \geqslant 0$ and is zero otherwise and

$$p_i^{\mathrm{A}} = \sum_{j\,NNi} \left(\frac{\underline{F}_{ij}^{\mathrm{AA};\varsigma_m=0}}{A_{ij}} \frac{\underline{r}_i - \underline{r}_j}{|\underline{r}_i - \underline{r}_j|} \right)$$

is a measure of the stress of A-type cell i by external forces not taking into account the adhesion of cells. The term mimics the case when cells can distinguish neighbor cells of their own type from neighbor cells of a different type and move in order to relax the compression within cells of their own type. If we would consider in the calculation of p_i^{A} also forces between A-type cells and B-type objects, then the effect at the interface between A-type cells and the B-type object would become negligibly small.

2. By the addition of a constant force term directed into the local outward-normal of the border of A-cells. In this case, $\underline{F}_i^{\mathrm{active,A}} = \underline{f}_i^{\mathrm{active,A}} + \underline{F}_i^{\mathrm{directed,A}}$.

$\underline{f}_i^{\mathrm{active,A}}$ is the random component of the active force obeying the same relations as in case 1. $\underline{F}_i^{\mathrm{directed,A}} = \frac{-\nabla p_i}{|\nabla p_i|} F_0$ with F_0 being the deterministic component of the active force, i.e. the cell moves with a deterministic force into the opposite direction of the local pressure gradient.

Some authors (see, e.g., [57]) assume that migrating cells try to adopt a certain target speed $\underline{v}_0$. This can be taken into account by replacing in the first term of the equation of motion $\underline{v}_i \to \underline{v}_i(1 - |\underline{v}_i|^2/v_0^2)$ for $|\underline{v}_0| > 0$. We will not consider this case here but note that it can be easily included in our concept.

For *B-type objects* we consider two cases: If B-objects are considered to be cells, then we assume that the active term $\underline{F}_i^{\text{active,B}}(t)$ is mimicked in the same way as for A-type cells in case 1, i.e. as an unbiased active random movement. If B-objects represent granular particles, we assume that the active force is zero, $\underline{F}_i^{\text{active,B}}(t) = \underline{0}$.

Multi-cellular spheroids. In the last part of the paper, we consider multi-cellular spheroids, i.e. 3D cell aggregates. The tissue architecture of (3D) multi-cellular spheroids is usually closer to the *in vivo* situation and shows the formation of extensive ECM (see, e.g. [58]). For example, staining for collagen V in SK-MES-1 cells, a non-small-cell lung cancer cell line shows massive ECM presence [59]. If this 3D network of ECM is stiff enough, it may allow cells to anchor and move as described in [51]. In this case the interpretation of the terms remains the same as that in the monolayer situation. The factor '4' in the autocorrelation function is then replaced by '6' ($= 2d$; d is the space dimension) and the diffusion is assumed to be isotropic (we use diffusion constant D). However, some multi-cellular spheroids show only a very sparse matrix. In this case, the main component of active migration occurs from forces exerted from a cell on its neighbor cells (i.e. not on the ECM anymore). Those forces are balanced by the respective reaction forces of the neighbors on that cell. Stochastic forces from one cell on its neighbor cells may also emerge from fluctuations of the cells' membranes in which case also momentum is conserved; hence, the random force terms for neighbor cells have to balance each other. Taking this into account would modify the equations of motion slightly but the results would not be expected to show any major changes for the situations presented in this paper. (i) We are here interested in pattern formation on long time scales compared to the characteristic times of the stochastic fluctuation terms representing the cell micro-motility and, as the spheroids are embedded in a dense arrangement of granular objects and not swimming in liquid suspension, cells do not detach and move away as a consequence of the random movement. (ii) For multi-cellular spheroids we consider below pushing-type movement emerging from cell proliferation. Here active directed movements are not considered and small fluctuation forces do not play a role.

That the precise form of the noise terms representing the micro-motility does not play a role is supported by the simulation results at varying micro-motility of the B-objects shown in figures 6(A)–(D), suggesting that the random component in the movement of cells has statistically no effect on the formed pattern for the situations considered in this paper. However, it might be worth noting that the movement of the cells in liquid suspension could be mimicked in the same framework: cell movements due to collisions with fluid particles generate a random Brownian movement component, usually with smaller amplitude than for active random movement, so in this case the equations of motions are the same as explained above but with a smaller diffusion constant.

Overview of simulations. In our simulations below, we consider one-layer-thick monolayers. For A-type cells the initial number at the start of the simulation at $t = 0$ is always $N(t = 0) = 1$.

In the first part we investigate the effect of pushing/pulling-type movement on the growth kinetics of a monolayer not embedded in another external material of B-type objects.

In the second part, we consider an expanding monolayer in an embedding material of B-type objects (granular objects or cells). We vary the following parameters: (i) motility (diffusion constant) and mobility (friction constant) of the embedding medium, (ii) density of the embedding objects, (iii) elasticity of the embedding objects, (iv) adhesion strength of the embedding objects, (v) object size of the embedding objects and (vi) cytolysis versus no cytolysis of apoptotic cells of the expanding clone. The reference parameters used in the simulations are given in table 1.

Table 1. Reference parameters.

Parameter/symbol	Unit	Value (range in sensitivity analysis)	Source
Cell diameter l	μm	15	Assumed
Intrinsic cell cycle time τ	h	18	[86]
Reference energy F_{T}	J	10^{-16}	[50, 56]
Young's modulus E_{A}, E_{B}	Pa	450 (300–1000)	[77, 78]
Poisson ratio υ	–	0.4	[87, 88]
Diffusion constant D	$\mathrm{cm}^2\,\mathrm{s}^{-1}$	10^{-12}	[56]
Receptor surface density ς_m, ς_{AA}	m^{-2}	10^{15}	[83, 84]
Receptor surface density ς_{AB}, ς_{BB}	m^{-2}	0	[83, 84]
Binding energy single bond W_{s}		$\approx 25 k_{\mathrm{B}} T$	[56]
Friction coefficient γ	$\mathrm{Ns\,m}^{-3}$	10^7	Assumed
Diameter of environment	mm	1.6 (0.25–2.4)	

In the third part, we consider 3D multi-cellular spheroids in an embedding material of granular objects and compare our simulation results directly with the findings of Helmlinger *et al* [1] and Galle *et al* [60]. We from now on always use D to denote the diffusion constant. For monolayers, this corresponds to using the symbol D instead of $D_{\parallel}$.

To quantify our simulation results, we measure the cell population size $N(t)$, and the radius of gyration,

$$R_{\mathrm{gyr}} = \sqrt{\frac{1}{N}\sum_i (\underline{r}_i - \underline{R}_{\mathrm{CM}})^2},$$

where $\underline{R}_{\mathrm{CM}} = \frac{1}{N}\sum_i \underline{r}_i$ is the position of the center of mass. The sums run over the expanding (the growing) clone. If the monolayer is compact with a circular border, then $R = \sqrt{2} R_{\mathrm{gyr}}$, where R is the radius of the monolayer. For this reason, we usually display R or the diameter, $L = 2R$, calculated from the radius of gyration. In addition, we store the full spatial–temporal configuration of cells and objects at different times during the growth process.

3. Results

3.1. Reference situation: growing monolayers without an embedding medium

In [46], the authors found an active migration of cells towards the free edge of an expanding monolayer culture. Hoehme *et al* [45] found that an active migration of cells towards a drug-induced necrotic zone is necessary for explaining regeneration of liver after toxic damage.

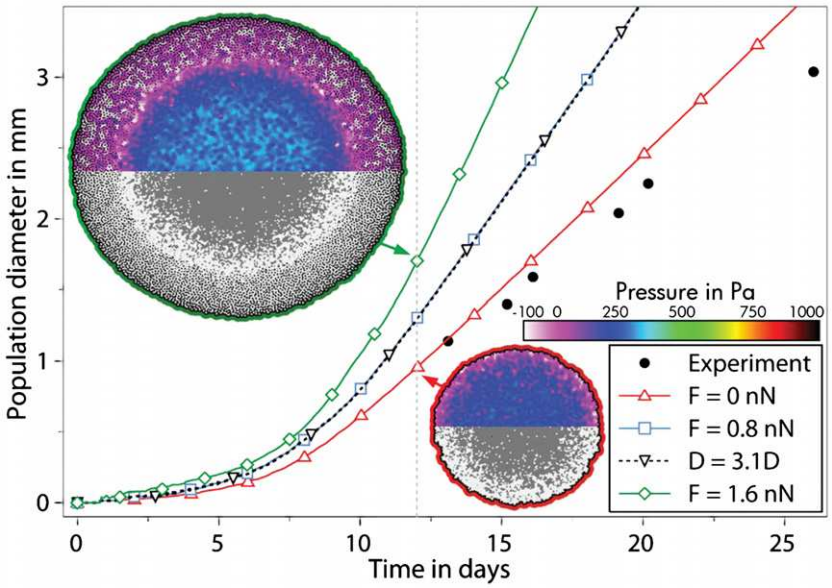

Figure 2. Diameter of the monolayer in the free environment versus time for different motility models. The black points denote the results experimentally found for rat astrocytes in [61] denoting an expansion speed in the linear growth regime of about $6\,\mu\mathrm{m\,h^{-1}}$. Typical values for the expansion speed of monolayers for different cell lines span 2–$23\,\mu\mathrm{m\,h^{-1}}$ [62]. The red curve (up triangles) denotes case 1: uniformly distributed micro-motility (with no bias). The full blue and green lines (diamond and square) result from uniformly distributed micro-motility plus a directed force term of either 0.8 or 1.6 nN. For an explanation see case 2(ii) for the active cell migration term of A-cells. The black dashed curve (down triangles) denotes biased micro-motility as defined for case 2(i). Here, $D_{\mathrm{A}} = 3.1 D_0$. Insets: if a cell actively moves into the free space around the monolayer, the cell density in the surface region is smaller (upper left inset) than if active migration is purely random (lower right inset). Active migration accelerates monolayer expansion. In the lower half, white cells are proliferating and gray cells are in G_0 phase.

Figure 2 shows the results of a biased and an unbiased micro-motility in a growing one-cell-thick dense monolayer. The strength of the bias has been varied up to the size at which cells detach.

As B-type objects are not considered in this part, and as $\underline{F}_{iS}^{\mathrm{AS}}$ is approximately constant by construction, the variable part of the pressure is given by

$$p_i^{\mathrm{tot}} \approx \sum_{j\,NN\,i} \left(\frac{\underline{F}_{ij}^{\mathrm{AA}}}{A_{ij}} \frac{\underline{r}_i - \underline{r}_j}{|\underline{r}_i - \underline{r}_j|} \right).$$

The results show an acceleration of growth which can be explained by an increase of the proliferating rim by the biased cell micro-motility. Due to the active movement towards the free edge of the monolayer the cell–cell contacts are stretched. This leads to a reduction of cell compression and thereby facilitates reentrance of cells into the cell cycle. Moreover, the cell

density close to the border is smaller for biased than for unbiased micro-motility. We conclude that a bias in the micro-motility promotes the growth of a monolayer. We expect the same result for multi-cellular spheroids. Transferred to the case of a tumor in the soft tissue environment, any morphogen that biases micro-motility or an increase of its amplitude or both will promote the speed of growth of the expanding tumor. Besides this acceleration effect, we observe that biased micro-motility reduces the random motion of cells inside monolayers because cells in almost isotropic multi-cellular environments then have a smaller tendency to move. On the other hand, the micro-motility is larger close to the border.

So far we have used model rule 2 of figure 1 to mimic the cell cycle entrance control. Rule 1 of figure 1 has been tested in [24]. In figure 3, we test different hypotheses for cell cycle entrance, namely that the entrance into the cell cycle is triggered if $p_i^{\mathrm{tot}} < 0$, i.e. if normal stress $-p_i^{\mathrm{tot}}$ on the cell is positive (rule 3 in figure 1), and that cell cycle entrance only occurs if a cell is under stretch (rule 4 in figure 1). Note that for rule 4 it is sufficient if at least a single contact is stretched (i.e. $d_{ij} - (R_i + R_j) > 0$ for at least one $j \in \{j\}$) even if other contacts are under compression. It is not necessary that the cell is overall stretched into all directions (i.e. $\sum_j d_{ij} - (R_i + R_j) > 0$) or stretched into each direction (i.e. $d_{ij} - (R_i + R_j) > 0,\ \forall j$).

We again find that an increase of the active migration pulling force accelerates the growth. Above a certain pulling force (see the curve for 3 nN), cells detach and actively migrate into the environment. This is reflected in the radius of gyration versus time curve by the characteristic bump at about 2–3 days, indicating free migration (arrow in figure 3). However, the condition that cell entrance is possible only if a cell is under tension (positive normal stress) implies smaller growth velocities as for active directed migration forces and a positive pressure threshold (compression; implying negative normal stress) for the cell cycle entrance.

Interestingly, the largest and smallest growth speeds are observed for rule 3. The growth speed is largest for pulling forces of 1 nN or more and smallest in the absence of pulling forces. For rule 4, stochastic force fluctuations are able to trigger the overstretching of a single cell–cell contact for a moderate pulling force, resulting in a larger monolayer expansion speed than for rule 3.

In summary, the growth curve without any embedding medium shows that: (i) a directed force into the direction of the outwards-pointing interface normal leads to acceleration of growth compared to random uniformly directed micro-motility, (ii) a growth control mechanism permitting growth entrance only if a cell experiences a negative force slows down the growth speed for small pulling forces but accelerates it for large pulling forces, and (iii) a growth control mechanism that permits only cell cycle entrance for stretched cells leads to a smaller (larger) growth speed than for negative force control for large (small) pulling forces.

3.2. Growing monolayers in an embedding medium

In the following, the term 'embedding material' encompasses both the B-type cells and the B-type non-cellular objects. A distinction is made only if necessary.

Compared to earlier studies (see, e.g. [24, 26]), the introduction of an embedding material is an important step towards a modeling of the *in vivo* situation. We systematically modified the properties of the embedding material by varying the motility, initial density, elasticity, adhesion properties and average cell size of the embedding objects (B-type). We assumed the growing cells and the embedding material to be differentially adhesive with $\zeta_{\mathrm{m}} = \zeta_{\mathrm{AA}} = 10^{15}\ \mathrm{m}^{-2}$, where ζ_{AA} denotes the density of adhesion molecules in the case of an interaction between two cells of

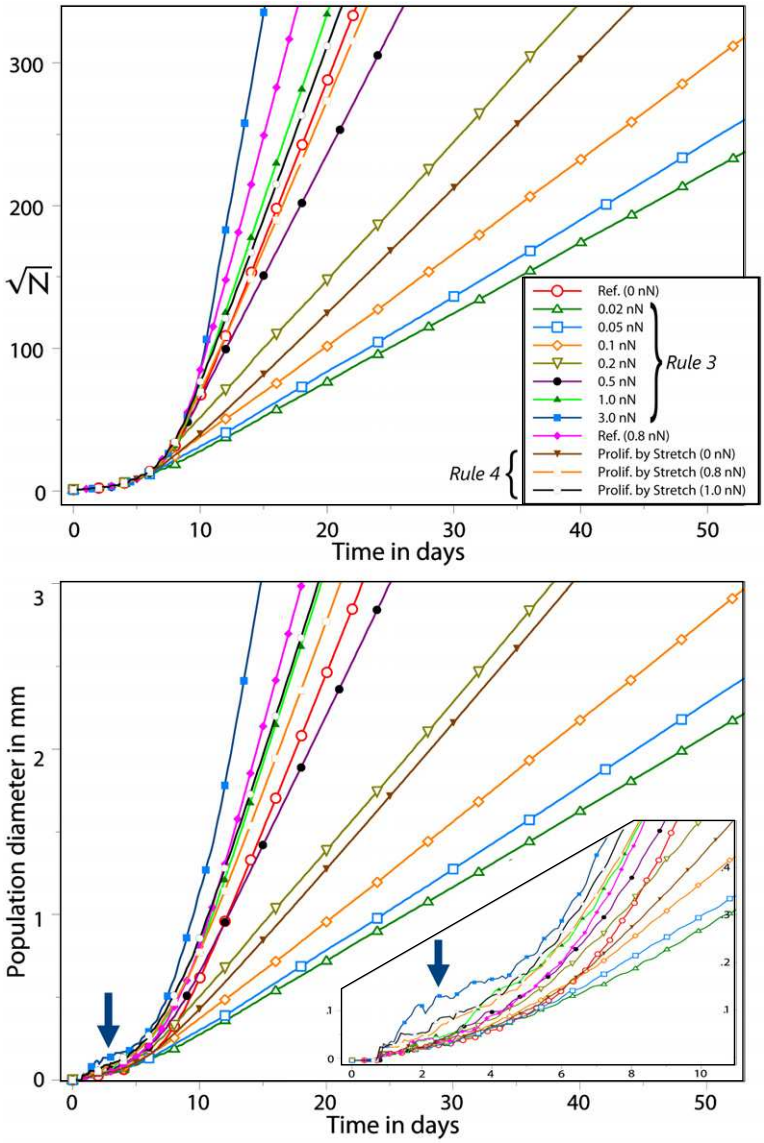

Figure 3. Square root of population size (top plot) and population diameter ($L = 2\sqrt{2}R_{\mathrm{gyr}}$, see above) (bottom plot) if cells move actively into the direction of the free edge according to the migration rule in case 2(ii) and different variants of cell cycle entrance control rules. (i) (Green triangles; blue open squares; light brown diamonds; up triangle brown/green; full black circles with brown lines; blue triangle with light green line; full blue square with blue line): cell division entrance occurs only if the force is attractive (negative; see rule 3 in figure 1). (ii) (Brown up triangle with brown line; dashed pink line; dashed black line): cell cycle entrance occurs only if the cell is stretched (see rule 4 in figure 1). For details see text. For comparison, the reference curve for a uniformly undirected active migration force (case 1) and positive pressure threshold for cell cycle entrance (red, hollow circles, see rule 2 in figure 1) as well as the curve with a directed active force of 0.8 nN (compare figure 2) and positive pressure threshold for cell cycle entrance (pink curve with a solid diamond shape) are shown. With

Figure 3. (Continued) increasing outwards-directed active migration force, the expansion velocity increases and for an active directed migration force of about 1 nN it becomes larger than the reference curve without the directed migration component. Beyond about 3 nN the cells detach and move freely. Note that the expansion speed for a directed micro-motility force of 0.8 nN and positive pressure threshold (= negative normal stress; pink curve) is larger than that for a directed micro-motility force of 1 nN if the cell cycle entrance is triggered by a negative pressure (= positive normal stress). The arrow shows the characteristic bump if cells detach. The bump denotes a regime where $R_{\mathrm{gyr}} \propto \sqrt{t}$ and is characteristic of the free random movement component (see also [63]).

type A. For B-objects we assume in most cases that $\zeta_{\mathrm{BB}} = \zeta_{\mathrm{AA}}$ so that the strength of adhesion between B-objects is the same as the strength of adhesion between A-cells. Furthermore, unless stated otherwise, we assume that A-cells and B-objects do not adhere, i.e. $\zeta_{\mathrm{AB}} = 0\,\mathrm{m}^{-2}$. The elastic moduli of A-cells and B-objects are denoted by E_{A} and E_{B}, respectively, and the diffusion constants for A-cells are denoted by D_{A} and for B-cells by D_{B}. Whereas $D_0 = 10^{-12}\,\mathrm{cm}^2\,\mathrm{s}^{-1}$ denotes the reference diffusion constant, γ_0 denotes the reference effective friction constant for cells with the substrate.

We started our simulations with a single cell of type A embedded in about 10^4–10^6 particles of the granular medium or model cells of type B. We used the number of embedding objects to control the initial density of the environmental objects. All elements of the embedding material were randomly arranged (isotropic homogeneously distributed) within a circular environment (figure 4) that was enclosed by a circular impermeable wall mimicking a virtual Petri dish. The initial placement of the B-objects on a regular square lattice was found to lead to symmetry artifacts in the emerging growth pattern. The shape of the impermeable wall fed back to the final shape of the growing aggregate (this was also experimentally observed in [1] for cell populations growing in a tube filled with agarose gel, see also figure 15), which is why we chose a circular border. The total area was held constant and was the same in all simulations. During the simulations, the growing population of cells of type A pushed away and compressed the surrounding objects. Figure 4 shows that a directed active migration component according to case 2 does not affect the growth speed of the expanding cell population as long as the directed force component is insufficient to cause detachment of cells from the expanding monolayer cell population.

For this reason, below we only consider pushing-type movement. We also consider the case when cell cycle entrance occurs only if $p_i^{\mathrm{tot}} > 0$. First we study growth without apoptosis and then include apoptosis with subsequent cytolysis.

Figure 5 shows the growth scenario with the reference parameter set.

3.2.1. Variation of the friction and motility of embedding objects. As a first step we analyzed the impact of varying the friction and micro-motility of the embedding objects of type B on the morphology of the expanding cell clone A.

As explained above, embedding granular objects are characterized by $D_{\mathrm{B}} = 0$, while embedding cells are characterized by $D_{\mathrm{B}} > 0$. For cells, the diffusion constant D_{B} and the friction coefficient γ^{BS} can be varied independently. A fluctuation dissipation theorem linking

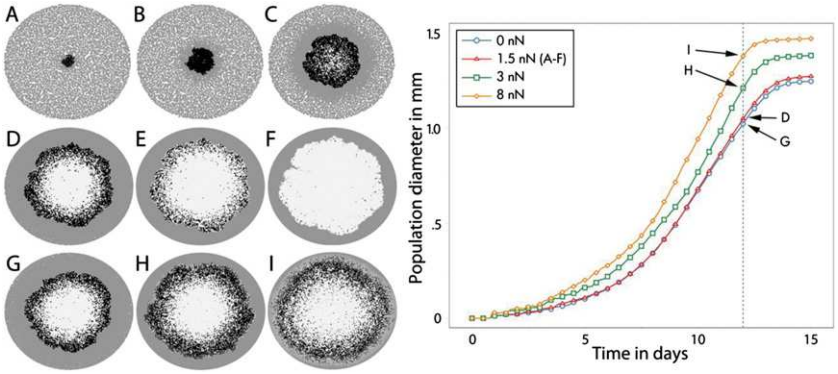

Figure 4. (A–F) Growth scenario for a directed active force of 1.5 nN after 6 (A), 8 (B), 10 (C), 12 (D), 13 (E) and 14 days (F). (G–I) Morphologies of corresponding populations for $t = 12$ days simulated with directed forces of 3 nN (H) and 8 nN (I) or no directed force (G). The embedding B-objects are colored gray, while proliferating A-cells are colored black and quiescent A-cells are colored white. Plot: growth scenarios (population diameter based on the radius of gyration). Note there is no difference as long as the active force is below the rupture force (blue curve with circle symbols and red curve with triangle symbols). Only if the active force is above the rupture force (green curve with square symbols and orange curve with diamond symbols), is the growth moderately accelerated and the saturation diameter elevated. As A-type cells are in an environment of B-type objects, not all cells are able to detach even if the directed active movement force amplitude F_0 is above the rupture force. Rather, the probability of rupture increases, leading to an increase of growth speed with increasing F_0. However, the differences in growth speed are far below that of a free monolayer (compare figures 2 and 3). In all simulations in this figure, $\gamma^{AS} = \gamma^{BS} = \gamma^{AA} = \gamma^{BB} = \gamma_O$.

strictly diffusion (fluctuation) with dissipation (friction) by a (thermal) temperature does not exist even though a formal analogy has been proposed [56]. Variations of the diffusion constant reflecting the micro-motility, an active motion component of the cell, may be caused by, for example, molecular changes in the complex coordinated cytoskeletal actions that are required for active cell movement [64]. Cell-substrate friction may be influenced by modification of the ECM, the liquid medium, or the covering of the dish surface.

For objects B of the embedding tissue, either the cell diffusion constant D_B or the friction γ^{BS} of cell type B with the substrate is modified.

While we found that a variation of D_B has only a negligible impact on the shape of the expanding multi-cellular population (figures 6(A)–(D)), we found that the variation of γ^{BS} leads to major changes in both growth velocity and population morphology (figures 6(E)–(H); figure 8(A) versus (C), figure 8(B) versus (D), figure 8(F) versus (H), figure 8(G) versus (I)).

At sufficiently high friction between B-objects and medium, the border of the A-clone forms dendrites. With increasing medium friction, the growth velocity of the expanding A-cell clone decreases (compare, for example, lines A and B in figure 11), and the critical wavelength (the size at which a domain splits into two branches so that dendrites form) decreases (figures 6(E)–(H)). Effectively such an increase of medium friction of the host tissue increases the

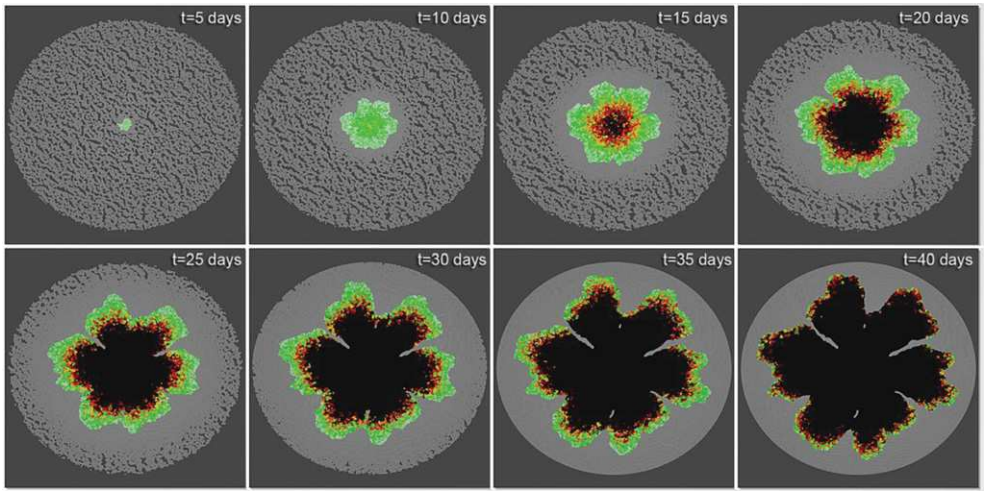

Figure 5. Illustration of multi-cellular growth embedded in tissue. The figure shows a growth scenario with the reference parameter set. The coloring of the growing cell population (cell type A) reveals the distribution of proliferation activity: cells of white color have divided within the average cell cycle time, whereas green cells have not divided for two times the average cycle time (yellow = 4 times, red = 6 times and black = more than 10 times). The coloring shows that proliferation mainly takes place at the population border. The embedding tissue (cell type B) is colored light gray. The parameters are: $E_A = E_B = 450\,\text{Pa}$, $\nu^A = \nu^B = 0.4$, $D_A = D_B = D_0$, $D_0 = 10^{-12}\,\text{cm}^2\,\text{s}^{-1}$, $\zeta_m = 10^{15}\,\text{m}^{-2}$, $\gamma^{AA} = \gamma^{BB} = \gamma^{AS} = \gamma_0$, $\gamma^{BS} = 5\gamma_0$, $\gamma_0 = 10^7\,\text{Ns}\,\text{m}^{-3}$, $\rho_B = \rho_0 = 5250$ cells per mm^2, $\zeta_{AA} = 10^{15}\,\text{m}^{-2}$, $\zeta_{BB} = \zeta_{AA}$; $\zeta_{AB} = 0\,\text{m}^{-2}$, $l_A = l_B = l_0 = 15\,\mu\text{m}$. $N_B = 20\,078$. See movie 1, available at stacks.iop.org/NJP/14/055025/mmedia.[3]

viscosity of the tumor micro-environment, which is reminiscent of a Saffman–Taylor-like instability [65], a viscous fingering.

The additional cell mass generated by cell proliferation generates a pressure gradient moving one 'fluid' (the expanding cell clone) against another 'fluid' (the extracellular objects). If the friction of the external objects with the dish (or a medium between the objects) is too large, they cannot move away with the same speed as the growth front. So cells of the growing clone expand and form fingers into small holes emerging by chance. At the tip of the dendritic fingers the local stress is smaller than that in the interior (figure 8(E)).

Another argument supporting the view of a viscous fingering instability is that simulation results of dividing isolated cell clones (not embedded in an external medium of B-objects) with the single-cell-based model used in this paper could be mimicked within a continuum description using mass conservation with a pressure-controlled growth term, $\partial_t n + \underline{\nabla} \cdot (n\underline{v}) = nH(p_0 - p)/\tau$ in combination with Darcy's law [66], $\underline{v} = -(k/\eta)\underline{\nabla} p$ [66]. Here, $n(\underline{r},t)$ is the local cell density, H the Heaviside step function, $\underline{v}$ the velocity of the expanding front at the border of the A-cell clone, τ the effective cell cycle time that depends also on the shape of the cycle time distribution [53], p the local pressure (probably better referred to as normal stress), k the permeability and η the viscosity. As the simulation results with the single-cell-based model

[3] A higher resolution version can be found at http://msysbio.com/videos_njp.

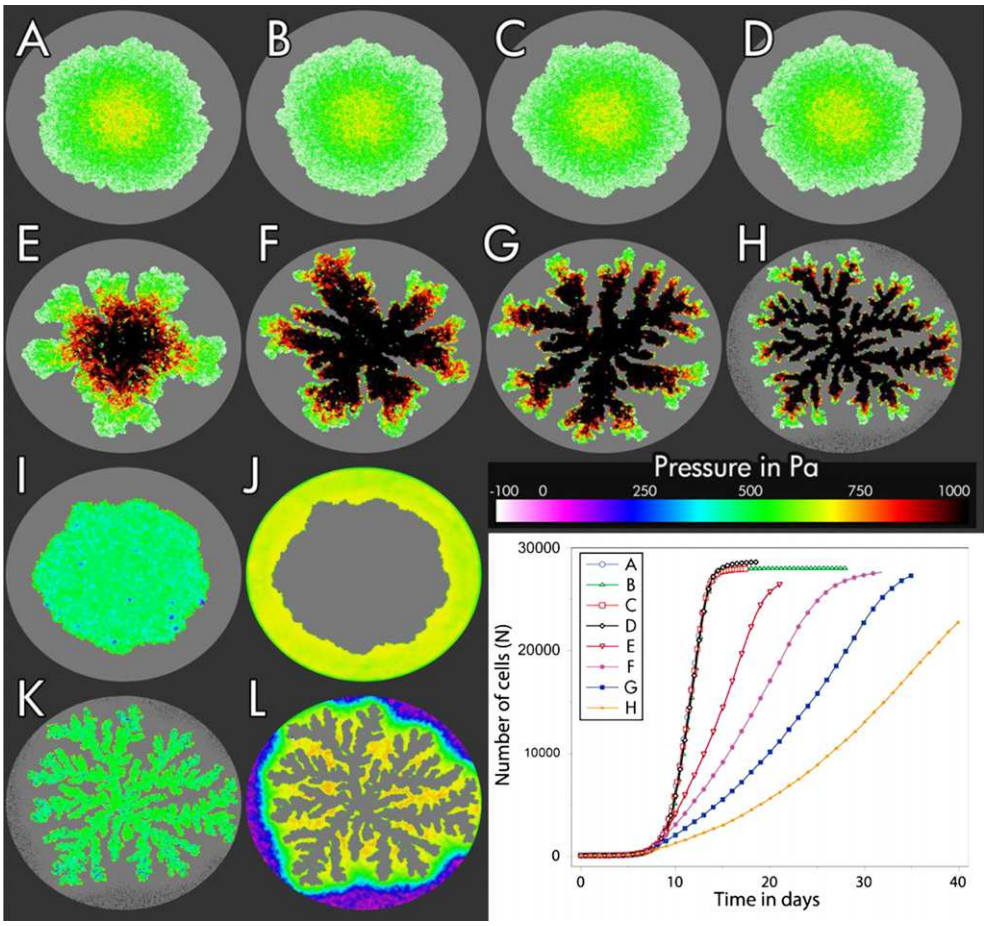

Figure 6. Impact of host tissue motility. (A–D) Compact tumor monolayers in 2D. (A) $D_B = 0$ (host tissue = granular medium), $\gamma^{BS} = \gamma_0$, (B) $D_B = 0.1D_0$, $\gamma^{BB} = \gamma_0$, (C) $D_B = D_0$, $\gamma^{BS} = \gamma_0$, (D) $D_B = 10D_0$, $\gamma^{BS} = \gamma_0$. (E–H) Increasingly dendritic tumor monolayers in 2D. (E) $D_B = D_0$, $\gamma^{BS} = 5\gamma_0$, (F) $D_B = D_0$, $\gamma^{BS} = 10\gamma_0$, (G) $D_B = D_0$, $\gamma^{BS} = 20\gamma_0$ (see movie 2, available at stacks.iop.org/NJP/14/055025/mmedia)[4], (H) $D_B = D_0$, $\gamma^{BS} = 50\gamma_0$, $\zeta_{BB} = 0$. (I) Pressure p^A (see the legend) exerted on A-cells in population C. (J) p^B in population C. (K) p^A in population H. (L) p^B in population H. The right inset shows $N_A(t)$. With increasing friction of the embedding B-type objects with the substrate, the growth speed of population A decreases.

in [66] suggested a step function-like cell density profile dropping sharply at the population border, accompanied by a less sharp decrease of the pressure p towards the population border, the state equation $n(p)$ looked to be a step-like function of n with a jump from zero density to the bulk density as $p > 0$ so $n(p)$ did not need to be considered explicitly. The adhesion between cells of the expanding clone (of cell type A) generates a cohesive force term, which can be related to a sort of surface tension σ. The friction between B-objects and the substrate is larger than between A-cells and the substrate. So the growing cell clone may be interpreted similarly to a radial Hele–Shaw cell in which a (less viscous) fluid is injected into a more viscous fluid,

[4] A higher resolution version can be found at http://msysbio.com/videos_njp.

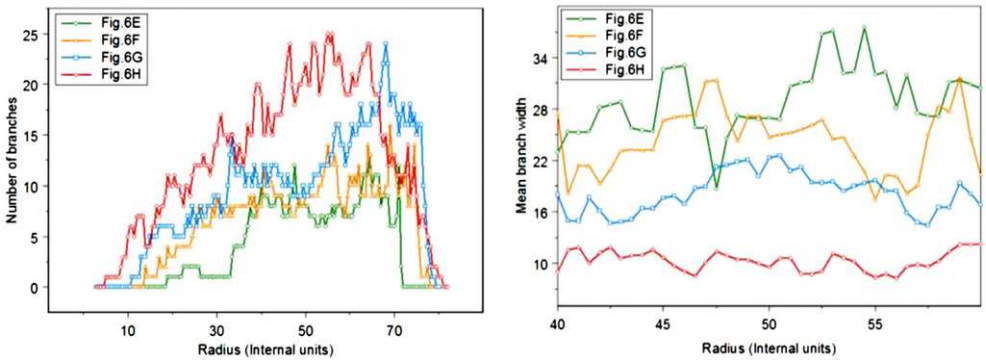

Figure 7. Quantitative analysis of morphology for varying friction. The number of dendritic fingers (A) and the mean branch size (B) at a specific distance R from the center of mass of the tumor cell population for the growth pattern in figures 6(E)–(H). $D_B = D_0$, $\zeta_{BB} = 0$. Red lines (see figure 6(E)): $\gamma^{BS} = 5\gamma_0$; blue lines (see figure 6(F)): $\gamma^{BS} = 10\gamma_0$; yellow line (see figure 6(G)): $\gamma^{BS} = 20\gamma_0$; green line (see figure 6(H)): $\gamma^{BS} = 50\gamma_0$.

the two fluids being constrained by two parallel plates. This is known to generate a viscous fingering instability (see, e.g. [34]).

Further support for this view emerges from an analysis of the branching pattern, which we exemplify for the simulations shown in figures 6(E)–(H) (see figure 7). In figure 7(A), we draw the number of branches with increasing distance to the center of mass, given by $\underline{R}_{cm} = \sum_{i=1}^{N} \underline{r}_i$. At too large distances, approximately $R > 50$, the number of branches decreases again as then the population of A-cells come close to the border. Up to this value, the mean branch width is approximately constant even for a single realization of the growth process (figure 7(B)).

Either by dividing the circumference at a distance R, given by $U = 2\pi R$ by the number of branches using the data in figure 7(A), or using the branch size from figure 7(B), one obtains a measure proportional to the domain size λ_{crit} at which an instability occurs. From a classical Saffman–Taylor instability, one would expect $\lambda_{crit} \propto 1/[v(\eta^{BS} - \eta_0)]^{1/2}$ where η_0 is the viscosity of a fluid of small viscosity expanding in another fluid with higher viscosity η^{BS}. v is the growth velocity of the expanding fluid usually noted as dR/dt. In order to test this relationship for growing cell populations, we replaced the difference of viscosities by the difference of the friction coefficients of cell-substrate friction for A-cells and B-objects ($\gamma^{BS} - \gamma_0$) assuming $\eta^{BS} \propto \gamma^{BS}$, $\eta_0 \propto \gamma_0$. We estimated v from $v \propto d\sqrt{N}/dt$ as a measure of the velocity of a growing front which can be calculated from the data on $N(t)$ presented in figure 6. However, we found that the current data are insufficient to confirm the classical relation for λ_{crit} even though the scenarios in figures 6(A)–(H) and the findings in figure 7 show the same qualitative tendencies as for a Saffman–Taylor instability. If one replaces the observed expansion velocity v by the intrinsic velocity v_0 of the expanding monolayer in the absence of the embedding B-objects, then we find approximately $\lambda_{crit} \propto 1/(\gamma^{BS} - \gamma_0)^{1/2}$. However, further simulations with larger systems and more realizations are necessary for identifying the precise relationships. These are very time consuming as the present simulations already took several weeks' simulation time.

After the instability has occurred, growth occurs almost only in the tip of the dendrites, even though a change in the width of the proliferating rim with increasing γ^{BS} could not be

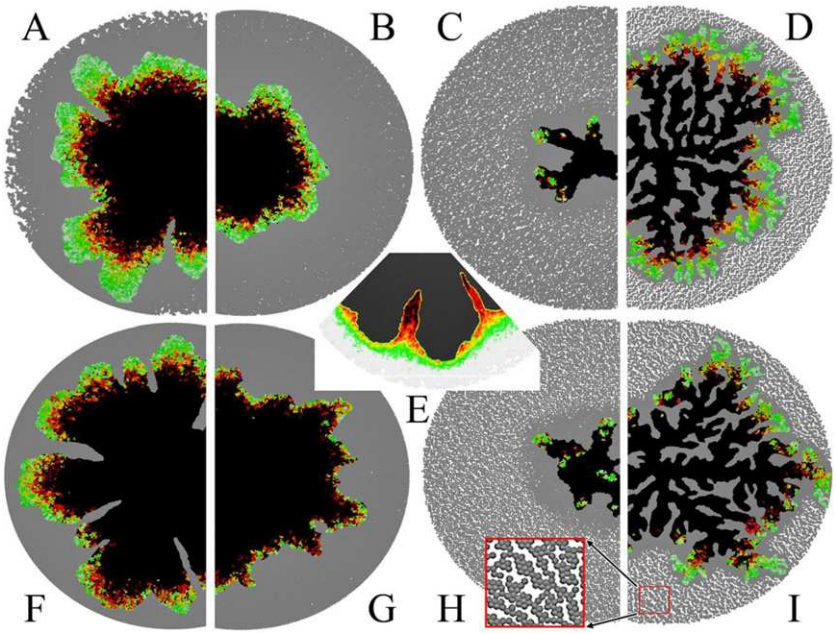

Figure 8. Impact of initial cell density and elasticity of tumor host tissue. Snapshots at the same time of the growth process for different parameter settings. $D_B = D_A = D_0$. (A) Simulation of a monolayer growing embedded in tissue (colored gray) of decreased initial cell density ($\rho_B \sim 3500$ cells per mm^2). (B) Tissue of increased density ($\rho_\beta \sim 7000$ cells per mm^2). (C) The same setting as (B) only with additionally increased medium friction of the embedding cells ($\gamma^{BB} = 20\gamma_0$). (D) The same as (A) but with increased host tissue medium friction ($\gamma^{BS} = 20\gamma_0$). (E) Alternative coloring of a section of (F) where tumor cells were colored black and embedding cells were colored according to the pressure exerted on them (black/red = high, yellow = medium, green = low). (F) Monolayer ($E = 450$ Pa) growing into the host tissue of lowered elasticity ($E_B = 300$ Pa). (G) The same as (F) with increased embedding tissue elasticity ($E_B = 1000$ Pa). (H) The same setting as (G) with additionally increased host tissue medium friction ($\gamma^{BS} = 20\gamma_0$). Red framed inset: magnification of embedding tissue: the adhesion between B-cells leads to a local spontaneous clustering. (I) The same setting as (F) with increased host tissue medium friction ($\gamma^{BS} = 20\gamma_0$). The coloring of tumor cells (A–D, F–I) shows their proliferation activity and corresponds to the description in the caption of figure 5. $\zeta_{BB} = \zeta_{AA}$.

observed (figure 8(A) versus figure 8(C), figure 8(B) versus figure 8(D), figure 8(F) versus figure 8(H), and figure 8(G) versus figure 8(I)). Due to the limitation of growth to the tip of the fingers, the total number of proliferating cells is reduced. Accordingly, the growth velocity of the expanding clone decreases with increasing friction of the embedding B-type objects with the medium, γ^{BS} (figure 11), as this leads to more branches (figures 6(E)–(H)). On the other hand, dendritic populations show a significant (+50%) increase of the radius of gyration at saturation compared to compact cell aggregates of A-type, reflecting that a dendritic structure results in a larger radius of gyration compared to a compact circular cell distribution at equal numbers of cells (compare also the growth curves for R_{gyr} and N in figure 11).

3.2.2. Variation of the host tissue cell density. In a further step, we varied the initial density of B-type objects by varying the number of B-type objects seeded around the A-type start cell. This is a relevant situation, as both *in vitro* and *in vivo* the average cell density varies from cell line to cell line and also depends on environmental factors, for example the local nutrient concentration or cytotoxic substances [67–69].

We studied initial cell densities (ρ_B) between 3500 and 7000 cells per mm^2, which encompasses the cell densities in many cell lines. The reference cell density (ρ_0) (see figure 5) was 5250 cells per mm^2.

An increase of the initial cell density in the host tissue ($\rho_B = 7000$ cells per mm^2) led to a significantly reduced expansion velocity of the growing monolayer, an earlier saturation of growth at a smaller diameter and a proliferating rim of smaller width during growth (figures 8(B) and 11).

Additionally, we studied the impact of the host tissue in case ρ_B and γ^{BS} were simultaneously varied. We found the influence of the discussed variations of ρ_B to be consistent, regarding the expansion velocity (figure 11), saturation size and width of the proliferating rim (figures 8(C) and (D)), with those reported above. The growth of a cell population embedded in host tissue of both increased medium friction ($\gamma^{BS} = 20\gamma_0$) and increased initial cell density ($\rho_B = 7000$ cells per mm^2) is highly inhibited (figure 8C).

On the other hand, comparison of figure 8(A) with (B) and of figure 8(D) with (C) indicates that only a moderate effect on the viscous fingering instability is caused by variations of the initial density (figure 8(D)) even though the critical wavelength λ_{crit} may be slightly smaller at higher densities of B-objects.

3.2.3. Variation of host tissue elasticity. Another important property of the tumor host tissue is its elasticity. For example, it has been found that tumors and their associated stroma have a lower elasticity (higher Young's modulus) than normal tissue [70] which enables them to more effectively compress and eventually collapse blood and lymphatic vessels in their vicinity [71] even though cancer cells themselves are usually softer than cells of the tissue they originate from [72].

In general, cell elasticity is largely determined by the biophysical properties of the cytoskeleton, a complex and dynamic cross-linked protein network anchored to the inner surface of the fluid lipid bilayer. Experiments suggest that cellular elasticity can be influenced by substances that depolymerize the cytoskeleton [73]. Furthermore, cellular elasticity is as closely coupled to dynamic cell behavior as cell movement, cell shape changes or cell division. However, the highly nonlinear elastic properties of a living cell are difficult to study and a detailed, experimentally validated model remains elusive. Nevertheless, the elasticity of the cytoskeleton can be measured by an increasing number of experimental techniques such as bulk rheology, traction force microscopy or atomic force microscopy [74–76].

In the simulations above, Young's modulus of the embedding objects E_B was chosen to be the same as Young's modulus E_A of the growing monolayer (type A) for which we assumed a Young's modulus of elasticity $E_A = E_0 = 450$ Pa [77, 78]. A decrease of Young's modulus from $E_B = 450$ Pa to $E_B = 300$ Pa leads to an increase of the proliferating rim and to a smaller critical wavelength (figure 8(F)), while an increase of Young's modulus of the embedding B-type objects (to $E_B = 1000$ Pa in figure 8(G)) leads to a decrease of the proliferating rim and a larger critical wavelength. Furthermore, a decrease of Young's modulus also leads to

increased growth velocity of the tumor accompanied by saturation at an increased population size (figure 11), reflecting that the resistance of the embedding objects is reduced.

If, in addition to the variation of E_B, the medium friction of the host tissue is increased ($\gamma^{BS} = 20\gamma_0$), we observe an amplification of the described influence (figures 8(H) and (I)). In case elasticity was decreased ($E_B = 1000\,\text{Pa}$) and the medium friction in the tumor microenvironment was simultaneously increased ($\gamma^{BB} = 20\gamma_0$), the growth of the tumor monolayer was found to be highly inhibited (figure 8(H)). Apparently, in this case the critical pressure threshold above which cells are not able to enter the cell cycle is reached quickly.

3.2.4. Variation of host tissue adhesivity. We further studied the impact of differential cell–cell adhesion [79, 80]. We consider changes of the adhesion strength of cells of the same type as well as between cell type A- and B-type objects. In general, intercellular adhesion is mediated by transmembrane proteins (selectins, cadherins and the immunoglobulin (Ig) superfamily). Except for the last, all of them require Ca^{2+} and Mg^{2+}. Therefore, many adhesive interactions are Ca^{2+} or Mg^{2+} dependent [69]. Moreover, in tumor spheroids, a significantly increased adhesion was found for $CoCl_2$-induced hypoxia, while ionizing radiation had an inverse effect [81]; hence adhesion is subject to changes.

In recent decades, many techniques have been developed to measure cellular adhesion; for example, Benoit *et al* [82] used a modified version of atomic force microscopy to measure adhesion forces between living cells and surfaces at the molecular level.

In our model the strength of the adhesive forces was determined by the density ζ_m of the corresponding receptors on the cell surface. As introduced before, we have usually chosen $\zeta_{AA} = \zeta_{BB} = 10^{15}\,\text{m}^{-2}$ [83, 84] and $\zeta_{AB} = 0\,\text{m}^{-2}$. Adhesion among B-type objects leads to the formation of patches with empty spaces in between if the density of B-type objects ρ_{BB} is not space-filling (figure 9(I), inset). The comparison of simulations without and with adhesion among B-type objects suggests a greater tendency towards finger formation if B-type objects adhere among each other (figures 9(A)–(C)) as the formation of fingers is facilitated in the free spaces between the patches. If the adhesion between A-cells and B-objects is stronger than A–A cell or B–B object adhesion, then inclusions of B-objects are observed in the expanding A-cell population (figure 9(F)). The adhesion between A-cells and B-objects, moreover, reduces the stress at the A–B interface compared to purely repulsive (Hertz) forces as in figure 9(D).

3.2.5. Variation of the average cell size of the host tissue. In the preceding sections the size (diameter) l_A of the growing tumor cells (type A) and the size l_B of the elements of the embedding tissue (B-type objects) were assumed to be identical ($l_B = l_A$). However, cell size is known to vary significantly between different cell types and tissues. Most eukaryotic cells have an average size (diameter) of 10–25 μm. However, the average cell size is not constant. It can be influenced by various factors, for example, cytotoxic substances [69] or genes involved in growth control [85]. The cell size of a specific cell line or tissue can, in general, be measured with bright field and laser scanning microscopy. In experiments using granular objects, the size of the objects can easily be varied. For these reasons, in this section we study the influence of the size of embedding B-type objects on the expanding A-type clone by varying the size of the B-type objects covering the range of typical eukaryotic cell sizes from 7 to 30 μm.

We find a decreasing tendency to form an instability with increasing object size (figures 10(A)–(D)). Perhaps, small objects can be more easily re-arranged than large objects.

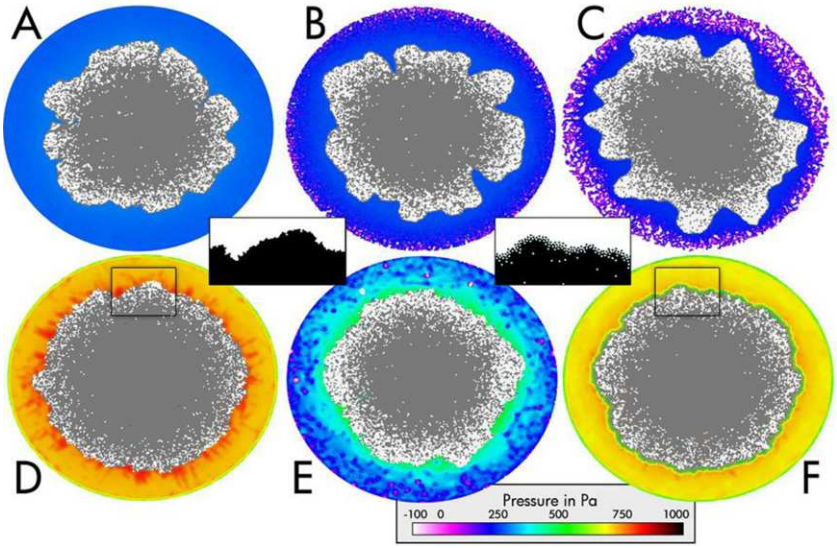

Figure 9. Impact of adhesion of the tumor host tissue. White cells: proliferating. Gray cells: quiescent. (A) $\zeta_{AA} = 10^{15}\,\mathrm{m}^{-2}$, $\zeta_{BB} = \zeta_{AB} = 0\,\mathrm{m}^{-2}$. Blue encodes the pressure. Dark blue: low; light blue: high pressure. (B) Reference situation $\zeta_{AA} = \zeta_{BB} = 10^{15}\,\mathrm{m}^{-2}$, $\zeta_{AB} = 0\,\mathrm{m}^{-2}$ (i.e. selective adhesion in host tissue). Colors denote pressure. (C) $\zeta_{BB} = 2\zeta_{AA} = 2 \times 10^{15}\,\mathrm{m}^{-2}$, $\zeta_{AB} = 0\,\mathrm{m}^{-2}$. In (A–C), $E_A = 450\,\mathrm{Pa}$. Lower three: (D–F) further variation of adhesion; (D) $\zeta_{AA} = \zeta_{BB} = \zeta_{AB} = 0$; (E) $\zeta_{AA} = \zeta_{BB} = \zeta_{AB} = 10^{15}\,\mathrm{m}^{-2}$; (F) $\zeta_{AA} = \zeta_{BB} = 0$, $\zeta_{AB} = 2 \times 10^{15}\,\mathrm{m}^{-2}$. The simulation time is the same in each figure. In (D–F), $E_A = 450\,\mathrm{Pa}$. Here, $N_B = 45\,180$ in an environment of diameter 2.4 mm.

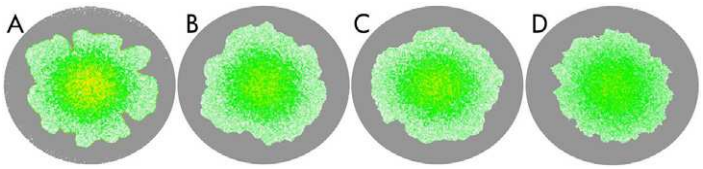

Figure 10. Impact of cell size in the embedding tissue. (A) $l_B = 7\,\mu\mathrm{m}$; (B) $l_B = 10\,\mu\mathrm{m}$; (C) $l_B = 15\,\mu\mathrm{m}$; (D) $l_D = 30\,\mu\mathrm{m}$. The number of cells has been calculated such that the space filling fraction is the same as that in the reference case (e.g. in figure 5) for all B-object sizes. $\zeta_{BB} = \zeta_{AA}$.

Furthermore, we found that larger embedding objects resulted in a slightly decreased expansion velocity, whereas smaller embedding objects led to a slightly increased growth velocity (not shown). In both situations, the width of the proliferating rim and the saturation size of the growing population remained unchanged. This can be explained by the larger finger formation if B-type objects are larger: as the A-type population grows mainly at the tip of the fingers, more (and smaller) fingers as found with increasing the size of B-type objects lead to an overall smaller number of proliferating cells, thereby reducing the expansion speed of the A-type cell clone. However, the effect of a stronger finger formation at smaller B-object size is surprising, because for infinitely small objects one might not expect a tendency towards stronger fingering. Further computational studies have been started to study this limit.

3.2.6. Apoptosis with cytolysis of apoptotic cells. Cytolysis, which is also designated as osmotic lysis, is a degenerative cellular process that involves the destruction of the outer cell membrane. This causes excess water to move into the cell and ultimately leads to the dissolution of the affected cell. Neighbor cells are able to phagocytize a dead cell. A majority of current assays for measuring cytolysis are based on the detection of changes in plasma membrane permeability and either the subsequent leakage of components (e.g. cytoplasmic enzymes) or uptake of dyes that are normally not able to enter the cell (e.g. Trypan blue or propidium iodide).

In our model, we introduced cytolytic processes to validate the robustness of our findings from preceding sections in a more dynamic and regenerative environment.

In order to model cytolysis, we assumed that after a certain time Δt_{cl}, apoptotic tumor cells are completely dissolved. In comparison with the preceding sections, where the main fraction of cell proliferation took place at the borders of the population, the introduction of cytolysis led to much more complex and highly dynamic proliferation activity patterns (figures 12(A) and (B)). Snapshots shown in figures 12(A) and (B) reveal proliferating regions (colored white) even in the interior of the tumor cell cluster. In this situation of constant cell renewal, no tumor cells remained arrested in G_0 for a long time (as for example those colored red or black in figure 12). The reason for this was that densely packed cells in G_0 became apoptotic and then were removed by cytolysis after Δt_{cl}. Thereafter surviving tumor cells in the vicinity of recently dissolved cells (black in figures 12(A) and (B), see arrows) were able to migrate into the free space and re-enter the cell cycle because of temporarily lowered cell density and thus lowered pressure (figures 12(E) and (F)). Cytolysis largely destroys (figures 12(C) and (D)) the typical layered proliferation pattern (e.g. figure 5) of growing cell populations.

Furthermore, the constant cell renewal introduced oscillations into the growth kinetics (figure 11, lines L). Importantly, the radius of gyration remains largely the same as for the corresponding simulations without cytolysis (figure 12, upper part). Moreover, we found no further changes of any of the previously described biomechanical influences of the tumor host tissue on the morphologies and growth dynamics of tumor cell populations. We therefore consider the results presented in previous sections to be robust and especially not depending on cell proliferation to be confined to the border of a multi-cellular population.

3.2.7. Growth and apoptosis in the expanding clone and host tissue. Finally, we considered the case of embedding cells capable of proliferation and apoptosis as for the expanding clone testing the idea of a homeostatic pressure proposed in [15]. We model this process in several steps. Firstly, the A-type clone was grown in the embedding medium of B-type cells suppressing cell proliferation and death until the A-type clone had a size of about $N = 10\,000$ cells, which was the case at a gyration radius of about 950 μm (figure 13). Then we introduced a relaxation phase (blue curve in figure 13). At about $t = 15$ days we restarted the simulation with now both the A-type cells and the embedding B-type cells proliferating and undergoing apoptosis. Both, cell cycle entrance and cell apoptosis, were triggered by a pressure threshold. At the first pressure threshold, a cell becomes quiescent, and at the second pressure threshold that was larger than the first threshold, it becomes apoptotic. We consider two cases. Firstly, we assume that the thresholds are pairwise the same for A- and B-type cells ($p_{\mathrm{A}}^{\mathrm{quiesc}} = p_{\mathrm{B}}^{\mathrm{quiesc}} = 300\,\mathrm{Pa}$; $p_{\mathrm{A}}^{\mathrm{apopt}} = p_{\mathrm{B}}^{\mathrm{apopt}} = 400\,\mathrm{Pa}$). This leads to a homeostatic situation (figure 13, green line). If, however, the apoptosis pressure threshold for B-cells is below the apoptosis pressure threshold for A-cells ($p_{\mathrm{A}}^{\mathrm{quiesc}} = 300\,\mathrm{Pa}$; $p_{\mathrm{A}}^{\mathrm{apopt}} = 400\,\mathrm{Pa}$; $p_{\mathrm{B}}^{\mathrm{quiesc}} = 200\,\mathrm{Pa}$; $p_{\mathrm{B}}^{\mathrm{apopt}} = 300\,\mathrm{Pa}$), the A-cell population slowly eliminates the B-cell population (orange line in figure 13). In this

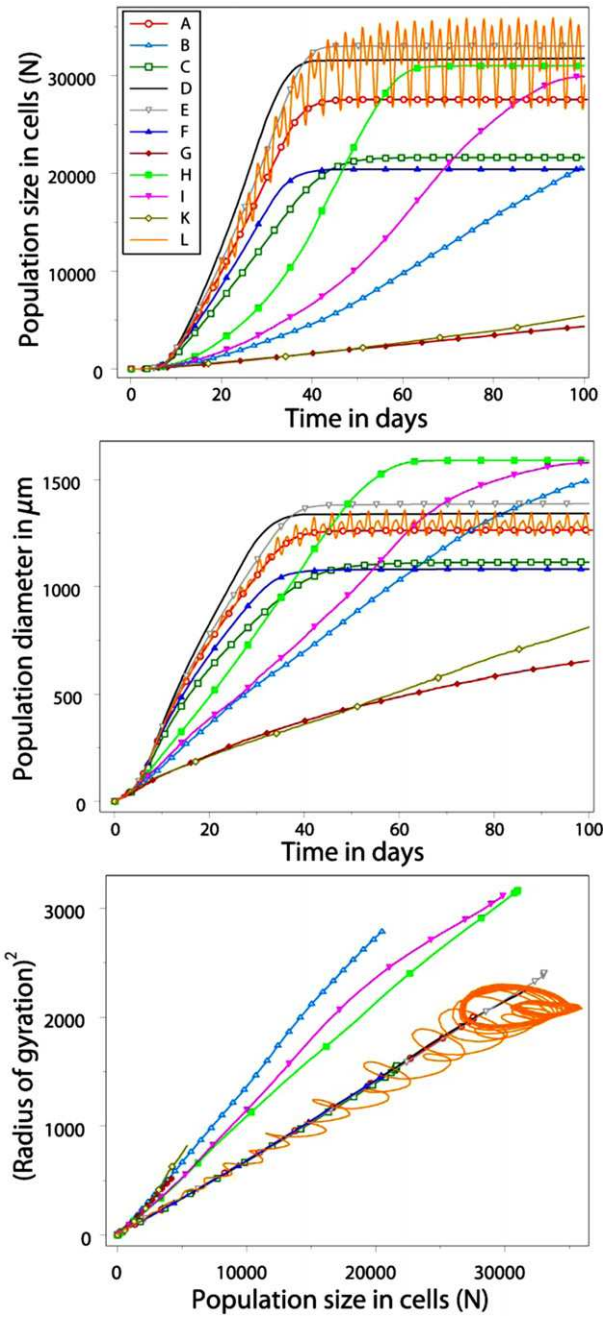

Figure 11. Comparison of growth kinetics in 2D. Top panel: the A-cell population size; middle panel: the population diameter $L = 2\sqrt{2}R_{\mathrm{gyr}}$; bottom panel: R^2_{gyr} versus N. (A) Curve 'A' (red line, empty circle symbol): the reference simulation. $D_{\mathrm{B}} = D_0$, $\gamma^{\mathrm{BS}} = \gamma_0$, $\rho_{\mathrm{B}} = \rho_0 = 5250$ cells per mm^2, $E = 450$ Pa, $E_{\mathrm{B}} = 450$ Pa, no selective adhesion was assumed and no cytolysis occurred. Curve 'B' (light blue line, empty up triangle symbol): increased host tissue medium friction ($\gamma_{\mathrm{T}} = 20\gamma_0$). Curve 'C' (green line, empty square symbol): increased initial cell density in the embedding tissue ($\rho_{\mathrm{B}} \approx 7000$ cells per mm^2). Curve 'D' (black line, no symbol): decreased initial cell density in the host tissue

Figure 11. (Continued) ($\rho_B \approx 3500$ cells per mm^2). Curve 'E' (gray line, empty down triangle symbol): increased host tissue elasticity ($E_B = 300$ Pa). Curve 'F' (dark blue line, solid up triangle symbol): decreased host tissue elasticity ($E_B = 1000$ Pa). Curve 'G' (dark red line, solid diamond symbol): increased initial cell density and increased medium friction ($\rho_B \approx 7000$ cells per mm^2, $\gamma^{BS} = 20\gamma_0$). Curve 'H' (light green line, solid square symbol): decreased initial cell density and increased medium friction ($\rho_B \sim 3500$ cells per mm^2, $\gamma^{BS} = 20\gamma_0$). Curve 'I' (magenta line, solid down triangle symbol): increased host tissue elasticity ($E_B = 300$ Pa) and medium friction ($\gamma^{BS} = 20\gamma_0$). Curve 'K' (dark yellow line, empty diamond symbol): decreased host tissue elasticity ($E_B = 1000$ Pa) and increased medium friction ($\gamma^{BB} = 20\gamma_0$). Curve 'L' (orange line, no symbol): the reference simulation (A) with cytolysis. $\zeta_{BB} = \zeta_{AA}$. The differences in the order of the saturation size between the radius of gyration and the number of cells for the same parameters result from the shape of the cell aggregates. Dendritic cell populations have a larger gyration radius at the same cell population size than compact circular cell populations. (C) The largest deviations from a circular shape are for curves B, I, H for which $\gamma^{BS} = 20\gamma_0$, and for which significant finger formation could be observed.

way, our model simulation results are compatible with the concept of a homeostatic pressure introduced in [15].

3.3. Growing multi-cellular spheroids in an embedding medium

In this section, we consider the growth of multi-cellular spheroids in a B-type object environment. We assume that cells secrete ECM in which they are able to anchor and move. This line of argument is supported by the observation in SK-MES-1 multi-cellular spheroids which show the presence of collagen V in the region of the tumor spheroid. The equations of motion for this case are adapted to three dimensions. Our studies in this section are inspired by the findings of Helmlinger *et al* [1].

We again observe a fingering instability if the friction coefficient between B-type objects and matrix is much larger than for A-type cells and matrix, $\gamma^{BS} \gg \gamma^{AS} = \gamma_0$ (figure 14). We calibrated the initial density and size of the flask to mimic the modified degree of agarose by different initial densities of B-type objects. We made a comparison with the experimental growth curves of Helmlinger *et al* [1] for LS174T cell populations and of Galle *et al* [60] for WiDr cells.

(We find that the initial density of B-type objects determines the saturation size, while the size of the flask influences the slope.) The density of B-type objects at saturation is in each case about 6×10^5 B-objects per mm. The idea of this study was not to mimic in detail the constitutive relation of agarose but rather to demonstrate that the pressure-mediated cell cycle control mechanism is able to reproduce the kinetics of growing cell populations in media of different mechanical properties. The inset in figure 14 shows that removal of B-objects, resulting in a release of external mechanical stress on the A-cell population, leads to a continuation of growth of the A-cell population as observed experimentally in [1]. Our findings about the tumor growth kinetics are consistent with those found in a multi-phase continuum model of Chen

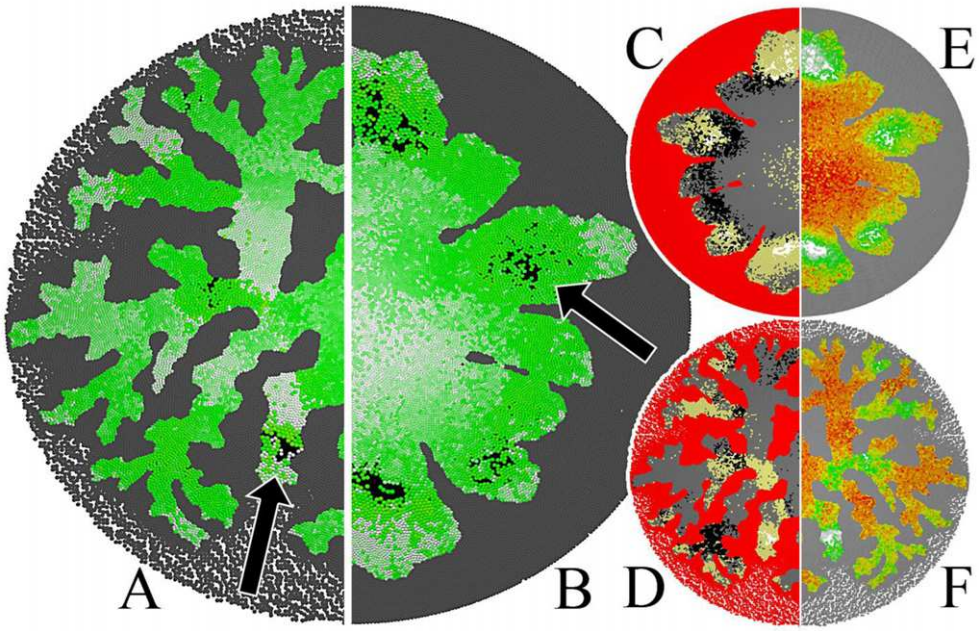

Figure 12. Impact of cytolytic cell renewal. (A) Tumor cell population growing into host tissue (gray) of increased medium friction ($\gamma^{BS} = 20\gamma_0$) with cytolysis after $\Delta t_{cl} = 12$ h. See movie 3, available at stacks.iop.org/NJP/14/055025/mmedia.[5] (B) Simulation as in figure 5 ($\gamma^{BS} = 5\gamma_0$) but with cytolysis. Black patches indicate areas where recently cells were dissolved and the empty space had not yet been filled by growing cells (black arrows). The coloring is equivalent to figure 5. See movie 4, available at stacks.iop.org/NJP/14/055025/mmedia.[5] (C/D) Alternative stainings of (A/B) where the host tissue is colored red, proliferating cells are colored ocher, quiescent cells are gray, apoptotic cells (before cytolysis) are black and the empty space remains white. (E/F) Alternative stainings of (A/B) where cells are colored according to their compression (red = high and green = low compression).

et al [20] already introduced above. However, assuming spherical symmetry the authors studied the time dependence of the radial coordinate. Moreover, also the experimentally observed effect of the shape of the flask on the spatial shape of the growing A-cell population can be reproduced (figure 15). Growth occurs in the direction which minimizes pressure.

4. Discussion

As pointed out in [61, 62], isolated monolayers show linear growth kinetics after an initial exponential growth phase. In previous work [24], we have shown that the linear growth kinetics of dense monolayers can be explained by cell proliferation as the main trigger for the movement of cells towards the monolayer edge and thereby for expansion of the monolayer. In that model the entrance of a cell into the cell cycle could occur only if that cell was not subject to too strong deformation. Proliferation-triggered movement leads to a pushing-type movement of cells.

[5] A higher resolution version can be found at http://msysbio.com/videos_njp.

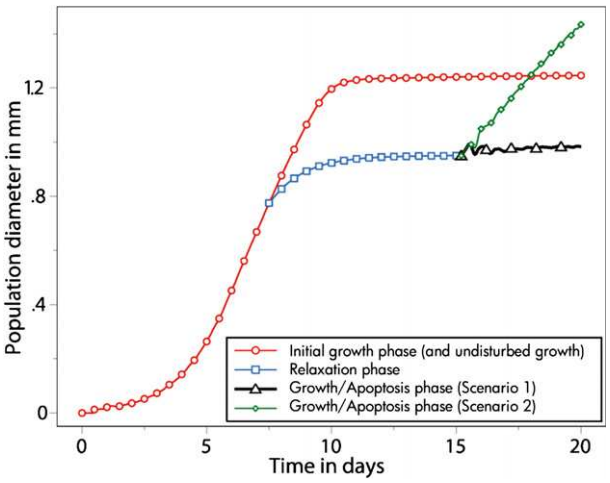

Figure 13. Growth and apoptosis of expanding clone and embedding medium. If the growth and apoptosis pressure thresholds are equal in the expanding A-type cell clone and the B-type embedding cells, the average size of both clones remains equal (black curve), while if the pressure at which B-cells undergo apoptosis is below the pressure at which A-cells undergo apoptosis, then the A-clone outcompetes the embedding B clone (green curve). The pressure-controlled cell cycle entrance and apoptosis mechanism thereby provides a possible representation of the concept of homeostatic pressure introduced in [15].

However, recent findings in [46] suggest that cell micro-motility may not be uniformly distributed but instead is directed towards the outwards-pointing normal of the monolayer border leading to traction of the cells. Cell proliferation was observed but the trigger of cell proliferation has not been studied. In order to probe key aspects of these observations, we studied in this paper an outwards-oriented active component of micro-motility modeled as a constant drift force on border cells in combination with three different growth control mechanisms: (i) a cell can only enter the cell cycle if the pressure on it is below a critical positive threshold. (ii) A cell can only enter the cell cycle if the total pressure is negative. (iii) A cell can enter the cell cycle only if it is stretched into the direction of at least one of its neighbor cells. We mimicked different mechanisms and found that the growth characteristics are very robust with regard to the qualitative dynamics, but the growth speed varies depending on the strength of the directed migration force component. Generally, a directed component in the micro-motility speeds up the monolayer expansion as the movement generates space for the dividing cells. In the case of control mechanism ((i); rule 2 in figure 1), even local patches of cells under tension (negative pressure) could be observed if the directed movement was sufficiently large; in the absence of such a force the cells are all under compression, so the pressure is positive. For the control mechanism ((ii); rule 3 in figure 1) the pressure is further reduced as only negative pressure is able to trigger cell cycle entrance. For the control mechanism ((iii); rule 4 in figure 1) the movement is a pulling movement: only if cells are stretched, are cells able to enter the cell cycle, leading to a further reduction of the local pressure. In both (ii) and (iii), the pressure at the border was negative. However, if entrance into the cell cycle occurs only if cells experience tension (case (ii)), or if they are stretched

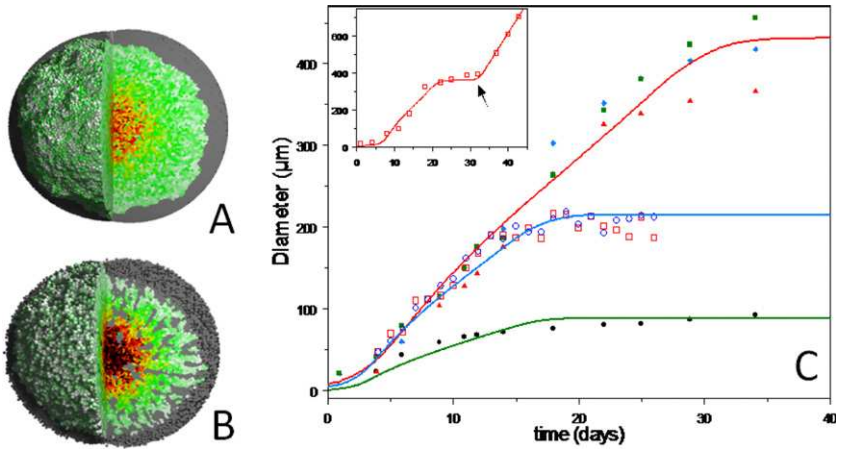

Figure 14. (A, B) Typical growth pattern in three dimensions for (A) $\gamma^{\mathrm{BS}} = \gamma^{\mathrm{AS}}$ and (B) $\gamma^{\mathrm{BS}} = 20\gamma^{\mathrm{AS}}$. See movie 5(A) and movie 6(B), available at stacks.iop.org/NJP/14/055025/mmedia.[6] (C) Experimental data of Helmlinger *et al* [1] for LS174T spheroids: 1.0% agarose gel (filled black circles), 0.8% agarose gel (filled red triangles), 0.5% agarose gel (filled blue diamonds) and 0.3% agarose gel (filled green squares). Model simulation referring to LS174T spheroids using $\rho_0 = 611 \times 10^3\,\mathrm{cells\,mm^{-3}}$ and a flask diameter of 500 μm (green line) and $207 \times 10^3\,\mathrm{cells\,mm^{-3}}$ (red line) and a flask diameter of 500 μm. Experimental data of Galle *et al* [60], WiDr spheroids: 5.0% agarose gel (red squares) and 2.5% agarose gel (blue circles). Blue line: model simulation referring to WiDr spheroids, $\rho_0 = 225 \times 10^3\,\mathrm{cells\,mm^{-3}}$ with a flask diameter of 250 μm. Inset: experimental data on growth alleviation by Helmlinger *et al* [1] for 0.7% agarose gel (symbols) and model simulation (line) using $\rho_0 = 215 \times 10^3\,\mathrm{cells\,mm^{-3}}$, a flask diameter of 500 μm and removal of embedding cells at $t = 30$ days. For all simulations in (C), $\gamma^{\mathrm{BS}} = \gamma^{\mathrm{AS}}$.

(case (iii)), this slows down the monolayer growth speed compared to a re-entrance as long as cells are not too much compressed (case (i)).

In the second part of the paper, we considered a growing population of cells embedded in a population of either granular objects or cells in order to study the emerging growth pattern. In this case, a directed movement had almost no consequence as long as the directed force component did not lead to rupture of the cell–cell contacts of the expanding cell clone.

We calculated until the growing clone enclosed by other objects had a population size of about 30 000 cells and varied the parameter values of the model over physiologically reasonable ranges. At this population size we could observe a viscous fingering instability which was particularly pronounced if the friction of the B-objects with the substrate was much larger than the friction between A-cells and the substrate. With increasing friction, the critical wavelength decreased. Moreover, the fingering pattern was moderately increased with increasing object size of the external medium as well as for increasing adhesion with between B-type objects. The micro-motility of the external objects has no detectable influence on the instability, and the density of B-type objects seem to only influence the growth speed and the saturation size

[6] A higher resolution version can be found at http://msysbio.com/videos_njp.

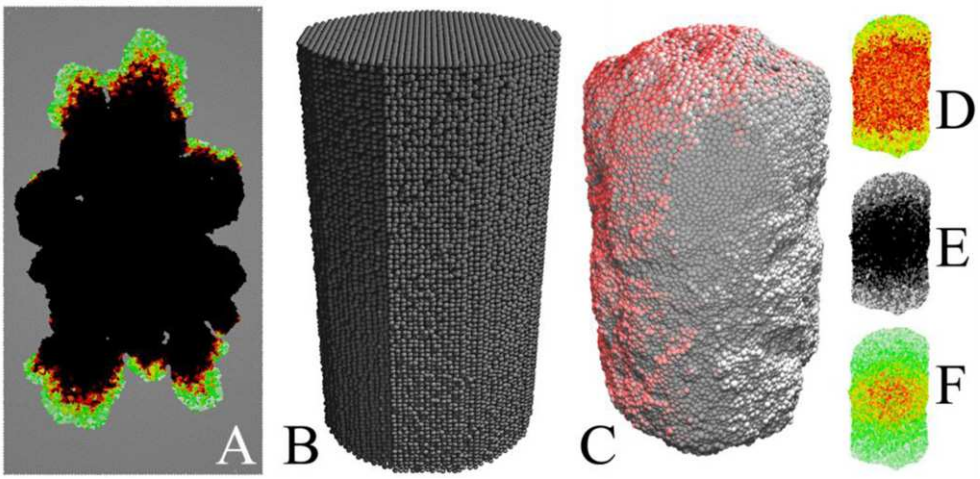

Figure 15. Impact of a flask shape on the shape of growing population. (A) 2D monolayer population growing in a rectangular area of embedding cells; the coloring of the cells is the same as in figure 2 (see movie 7, available at stacks.iop.org/NJP/14/055025/mmedia)[7]; (B) cylindrical environment (diameter = 1 mm) inducing non-uniform stress; (C) 3D multicellular spheroid of 2.5×10^5 with modulated (asymmetric) shape grown in (B). (D) Cross-section of (C) showing pressure exerted on cells (red = high pressure and green=low). (E) Cell vitality status (white = actively in cell cycle, gray = cell in G_0 phase and black = apoptotic area). (F) Proliferation activity, the coloring of the cells is the same as in figure 6.

of the population but not the fingering pattern. Moderate changes of Young's modulus from 300–1000 Pa mainly reduce the expansion speed of the growing clone. Even apoptosis, triggered if the local pressure overcomes a critical value, almost does not change the growth pattern. Instead, dying cells are quickly replaced by dividing neighbor cells.

We compared the relation for the critical wavelength of the instability with that of the Saffman–Taylor instability. Despite good qualitative agreement, larger systems will have to be studied to determine the quantitative dependence of the critical wavelength on the model parameters. These simulations are currently being performed, but they are very time consuming with one simulation running over several weeks to several months.

Recently, Basan and co-workers [43] considered the undulations at the interface between the epithelial tissue layer and the underlying stroma often observed in skin or mucosa. Epithelial cells flow towards the free surface from where they desquamate. Proliferation may trigger an instability as a consequence of shear between adjacent regions that becomes important as differences in the local epithelium height cause differences in the epithelial flow in adjacent regions. Higher proliferation, a higher local thickness of the proliferating layer and a higher epithelium viscosity each increase shear between adjacent regions, while, for example, a higher stroma viscosity stabilizes the interface. The latter is in contrast to our findings where higher viscosity in the environmental material facilitates the formation of fingers. Lowengrub *et al* [39] discuss an elastically induced splitting instability in which an elastic particle splits under deviatoric applied stress. They find that the onset and direction of the splitting instability

[7] A higher resolution version can be found at http://msysbio.com/videos_njp.

depends on the magnitude of both the misfit strain and applied stress as well as the details of the applied stress, the elastic constants and the initial shape of the particle. The results in figure 10 show that the size of the embedding objects affects the instability. Figure 9 shows that the strength of adhesion also matters. Hence it seems likely that the instability observed goes beyond the classical Saffman–Taylor instability despite the most prominent effect of the friction of A-cells and B-objects with the substrate.

In a next step, we considered birth and death in both the inner expanding clone and the embedding material, hence mimicking a competition process involving birth and death in the inner and the enclosing cell population. If we assume that the pressure threshold for birth in both populations is equal and the pressure threshold for death is equal, then the average population size of both populations remains the same, mimicking tissue homeostasis. If, however, the pressure threshold at which cells of the inner clone are still able to enter the cell cycle is equal to or larger than the pressure at which the embedding cells undergo apoptosis, then the inner cell population outcompetes the outer cell population. This observation is compatible with the recently proposed concept of a homeostatic pressure [15].

Finally, we considered $d = 3$ dimensions. Firstly, we noted that the fingering instability occurring with increasing friction of B-objects with the substrate can again be observed. Then we tested the impact of the initial B-object density on the growth kinetics and found that the growth kinetics corresponds to that found in [1] and [60] for cell clones growing in agarose gel.

We conclude that mechanical stress or strain-controlled cell cycle entrance mechanisms are able to explain many features of the growth pattern in monolayers and multi-cellular phenotypes both in the absence of a viscous or visco-elastic embedding medium and in its presence. The model predicts a fingering instability in a granular embedding medium which becomes particularly pronounced when the friction between the embedding objects and the medium between the embedding objects (the substrate) is increased.

Acknowledgments

DD gratefully acknowledges funding from the EU projects CANCERSYS and PASSPORT and the BMBF projects LUNGSYS and VLN (Virtual Liver Network). SH acknowledges funding from the EU project PASSPORT and the BMBF project VLN.

References

[1] Helmlinger G, Netti P A, Lichtenfeld H C, Melder R J and Jain R K 1997 Solid stress inhibits the growth of multicellular tumor spheroids *Nature Biotechnol.* **15** 778–83

[2] Koike C, McKee T D, Pluen A, Ramanujan S, Burton K, Munn L L, Boucher Y and Jain R K 2002 Solid stress facilitates spheroid formation: potential involvement of hyaluronan *Br. J. Cancer* **86** 947–53

[3] Forgacs G and Newman S A 2005 *Biological Physics of the Developing Embryo* (Cambridge: Cambridge University Press)

[4] Neagu A, Jakab K, Jamison R and Forgacs G 2005 Role of physical mechanisms in biological self-organization *Phys. Rev. Lett.* **95** 178104

[5] Shraiman B I 2005 Mechanical feedback as a possible regulator of tissue growth *Proc. Natl Acad. Sci. USA* **102** 3318–23

[6] Bischofs I B and Schwarz U S 2005 Effect of Poisson ratio on cellular structure formation *Phys. Rev. Lett.* **95** 068102-1–4

[7] Ingber D E 2005 Mechanical control of tissue growth: function follows form *Proc. Natl Acad. Sci. USA* **102** 11571–2
[8] Drasdo D 2000 Buckling instabilities in one-layered growing tissues *Phys. Rev. Lett.* **84** 4244–7
[9] Nelson C M, Jean R P, Tan J L, Liu W F, Sniadecki N J, Spector A A and Chen C S 2005 Emergent patterns of growth controlled by multicellular form and mechanics *Proc. Natl Acad. Sci. USA* **102** 11594–9
[10] Byrne H and Preziosi L 2003 Modelling solid tumour growth using the theory of mixtures *Math. Med. Biol.* **20** 341–66
[11] Ambrosi D and Preziosi L 2009 Cell adhesion mechanisms and stress relaxation in the mechanics of tumours *Biomech. Mod. Mechanobiol.* **8** 397–413
[12] Ambrosi D, Garikipati K and Kuhl E 1902 Mechanics in biology: cells and tissues *Phil. Trans. A: Math. Phys. Eng. Sci.* **367** 3335–7
[13] Galle J, Hoffmann M and Aust G 2009 From single cells to tissue architecture—a bottom-up approach to modelling the spatio-temporal organisation of complex multi-cellular systems *J. Math. Biol.* **58** 261–83
[14] Cheng G, Tse J, Jain R K and Munn L L 2009 Micro-environmental mechanical stress controls tumor spheroid size and morphology by suppressing proliferation and inducing apoptosis in cancer cells *PLoS One* **4** e4632
[15] Basan M, Risler T, Joanny J-F, Sastre-Garau X and Prost J 2009 Homeostatic competition drives tumor growth and metastasis nucleation *HFSP J.* **3** 265–72
[16] Ranft J, Basan M, Elgeti J, Joanny J-F, Prost J and Jülicher F 2010 Fluidization of tissues by cell division and apoptosis *Proc. Natl Acad. Sci. USA* **107** 20863–8
[17] Fritsch A, Höckel M, Kiessling T, David Nnetu K, Wetzel F, Zink M and Käs J A 2010 Are biomechanical changes necessary for tumour progression? *Nature Phys.* **6** 730–2
[18] Blanchard G B, Kabla A J, Schultz N L, Butler L C, Sanson B, Gorfinkiel N, Mahadevan L and Adams R J 2009 Tissue tectonics: morphogenetic strain rates, cell shape change and intercalation *Nature Methods* **6** 458–64
[19] Chaplain M A J, Graziano L and Preziosi L 2006 Mathematical modelling of the loss of tissue compression responsiveness and its role in solid tumour development *Math. Med. Biol.* **23** 197–229
[20] Chen C Y, Byrne H M and King J R 2001 The influence of growth-induced stress from the surrounding medium on the development of multicell spheroids *J. Math. Biol.* **43** 191–220
[21] Gartner M F, Fearns C, Wilson E L, Campbell J A and Dowdle E B 1992 Unusual growth characteristics of human melanoma xenografts in the nude mouse: a model for desmoplasia, dormancy and progression *Br. J. Cancer* **65** 487–90
[22] Vaage J 1992 Fibrosis in immune control of mammary-tumor growth *Int. J. Cancer* **51** 325–8
[23] Gordon V D, Valentine M T, Gardel M L, Andor-Ardó D, Dennison S, Bogdanov A A, Weitz D A and Deisboeck T S 2003 Measuring the mechanical stress induced by an expanding multicellular tumor system: a case study *Exp. Cell Res.* **289** 58–66
[24] Drasdo D and Hoehme S 2005 A single-cell-based model of tumor growth *in vitro*: monolayers and spheroids *Phys. Biol.* **2** 133–47
[25] Galle J, Loeffler M and Drasdo D 2005 Modelling the effect of deregulated proliferation and apoptosis on the growth dynamics of epithelial cell populations *in vitro Biophys. J.* **88** 62–75
[26] Drasdo D, Hoehme S and Block M 2007 On the role of physics in the growth and pattern formation of multi-cellular systems: what can we learn from individual-cell based models? *J. Stat. Phys.* **128** 287–345
[27] Hoehme S and Drasdo D 2010 Biomechanical and nutrient controls in the growth of mammalian Cell populations *Math. Population Stud.* **17** 166–87
[28] Radszuweit M, Block M, Hengstler J G, Schöll E and Drasdo D 2009 Comparing the growth kinetics of cell populations in two and three dimensions *Phys. Rev.* E **79** 051907
[29] Friedl P and Gilmour D 2009 Collective cell migration in morphogenesis, regeneration and cancer *Nat. Rev. Mol. Cell Biol.* **10** 445–57
[30] Ramis-Conde I, Drasdo D, Anderson A R A and Chaplain M A J 2008 Modeling the influence of the e-cadherin-beta-catenin pathway in cancer cell invasion: a multiscale approach *Biophys. J.* **95** 155–65

[31] Alberts B, Johnson A, Lewis J, Raff M, Roberts K and Walter P 2002 *The Cell* (New York: Garland Science)
[32] Weinberg R A 2007 *The Biology of Cancer* (New York: Garland Science)
[33] Ramis-Conde I, Chaplain M A J, Anderson A R A and Drasdo D 2009 Multi-scale modelling of cancer cell intravasation: the role of cadherins in metastasis *Phys. Biol.* **6** 16008
[34] Buka A and Kramer L 1995 *Pattern Formation in Liquid Crystals* (New York: Springer)
[35] Ben-Jacob E and Garik P 1990 The formation of patterns in non-equilibrium growth *Nature* **343** 523–30
[36] Pimpinelli A and Villain J 1998 *Physics of Crystal Growth* (Cambridge: Cambridge University Press)
[37] Lowengrub J and Cristini V 2004 Three-dimensional crystal growth. II. Nonlinear simulation and control of the Mullins–Sekerka instability *J. Cryst. Growth* **266** 2004
[38] Leo P H, Li S and Cristini V 2005 Nonlinear stability analysis of self-similar crystal growth: control of the Mullins-Sekerka instability. *J. Cryst. Growth* **277** 2005
[39] Lowengrub J, Leo P H and Nie Q 2001 On an elastically induced splitting instability *Acta Mater.* **49** 2761–72
[40] Goriely A and Ben Amar M 2005 Differential growth and instability in elastic shells *Phys. Rev. Lett.* **94** 198103–4
[41] Ben Amar M, Müller M M and Guven J 2008 Conical defects in growing sheets *Phys. Rev. Lett.* **101** 156104
[42] Dervaux J and Ben Amar M 2008 Morphogenesis of growing soft tissues *Phys. Rev. Lett.* **101** 068101
[43] Prost J, Basan M, Joanny J F and Risler T 2011 Undulation instability of epithelial tissues *Phys. Rev. Lett.* **106** 158101–4
[44] Ben-Jacob E, Cohen I and Levine H 2000 Cooperative self-organization of microorganisms *Adv. Phys.* **49** 395–554
[45] Hoehme S *et al* 2010 Prediction and validation of cell alignment along microvessels as order principle to restore tissue architecture in liver regeneration *Proc. Natl Acad. Sci. USA* **107** 10371–6
[46] Trepat X, Wasserman M R, Angelini T E, Millet E, Weitz D A, Butler J P and Fredberg J J 2009 Physical forces during collective cell migration *Nature Phys.* **5** 426–30
[47] Maruthamuthu V, Sabass B, Schwarz U S and Gardel M L 2011 Cell-ECM traction force modulates endogenous tension at cell–cell contacts *Proc. Natl Acad. Sci. USA* **108** 4708–13
[48] Chu Y-S, Dufour S, Paul Thiery J, Perez E and Pincet F 2005 Johnson–Kendall–Roberts theory applied to living cells *Phys. Rev. Lett.* **94** 028102
[49] Attard and Parker 1992 Deformation and adhesion of elastic bodies in contact *Phys. Rev.* A **46** 7959–71
[50] Schienbein M, Franke K and Gruler H 1994 Random walk and directed movement: comparison between inert particles and self-organized molecular machines 1994 *Phys. Rev.* E **49** 5462–71
[51] Wolf K, Wu Y I, Liu Y, Geiger J, Tam E, Overall C, Sharon Stack M and Friedl P 2007 Multi-step pericellular proteolysis controls the transition from individual to collective cancer cell invasion *Nature Cell Biol.* **9** 893–904
[52] Rosen P and Misfeldt D S 1980 Cell density determines epithelial migration in culture *Proc. Natl Acad. Sci. USA* **77** 4760–3
[53] Drasdo D 2005 Coarse graining in simulated cell populations *Adv. Complex Syst.* **8** 319–63
[54] Dickinson R B and Tranquillo R T 1993 A stochastic model for adhesion-mediated cell random motility and haptotaxis *J. Math. Biol.* **31** 563–600
[55] Dickinson R B and Tranquillo R T 1995 Transport equations and cell movement indices based on single cell properties *SIAM J. Appl. Math.* **55** 1419
[56] Beysens D, Forgacs G and Glazier J A 2000 Cell sorting is analogous to phase ordering in fluids *Proc. Natl Acad. Sci. USA* **97** 9467–71
[57] Vera Mikhailov C and Alexander S 2006 *From Cells to Societies* (Berlin: Springer)
[58] Santini M T and Rainaldi G 1999 Three-dimensional spheroid model in tumor biology *Pathobiology* **67** 148–57
[59] Mueller B and Mueller M 2011 Unpublished results from DKFZ
[60] Galle J, Aust G, Schaller G, Beyer T and Drasdo D 2006 Individual cell-based models of the spatio-temporal organisation of multicellular systems-achievements and limitations *Cytometry Teil* A **69A** 704–10

[61] Bru A, Pastor J M, Fernaud I, Bru I, Maelle S and Berenguer C 1998 Super-rough dynamics on tumour growth *Phys. Rev. Lett.* **81** 4008–11
[62] Bru A, Albertos S, Subiza J L, Lopez Garcia-Asensio J and Bru I 2003 The universal dynamics of tumour growth *Biophys. J.* **85** 2948–61
[63] Block M, Schoell E and Drasdo D 2007 Classifying the growth kinetics and surface dynamics in growing cell populations *Phys. Rev. Lett.* **99** 248101–4
[64] Walsh J E and Young M R 2008 Phosphatase regulation of cellular motility in the tumor microenvironment *FASEB J.* **22** 1029.9
[65] Saffman P G and Taylor G I 1958 The penetration of a fluid into a porous medium or Hele–Shaw cell containing a more viscous liquid *Proc. R. Soc.* **245** 312–29
[66] Byrne H and Drasdo D 2009 Individual-based and continuum models of growing cell populations: a comparison *J. Math. Biol.* **58** 657–87
[67] Blomquist E, Brunk U and Macieira-Coelho A 1993 The influence of cell co-operation, nutrients and surface area on cell division *Cell Prolif.* **26** 37–43
[68] Johansson N and Granéli E 1999 Influence of different nutrient conditions on cell density, chemical composition and toxicity of *Prymnesium parvum* (Haptophyta) in semi-continuous cultures *J. Exp. Mar. Biol. Ecol.* **239** 243–58
[69] Alberts B, Johnson A, Walter P, Lewis J, Raff M and Roberts K 2008 *Molecular Biology of the Cell* 5th edn (London: Taylor and Francis)
[70] Gieni R S and Hendzel M J 2008 Mechanotransduction from the ECM to the genome: are the pieces now in place? *J. Cell. Biochem.* **104** 1964–87
[71] Padera T P, Stoll B R, Tooredman J B, Capen D, di Tomaso E and Jain R K 2004 Pathology: cancer cells compress intratumour vessels *Nature* **427** 695
[72] Cross S E, Jin Y-S, Tondre J, Wong R, Rao J and Gimzewski J K 2008 Afm-based analysis of human metastatic cancer cells *Nanotechnology* **19** 384003
[73] Safran S A, Gov N, Nicolas A, Schwarz U S and Tlusty T 2005 Physics of cell elasticity, shape and adhesion *Physica* A **352** 171–201
[74] Guck J *et al* 2005 Optical deformability as an inherent cell marker for testing malignant transformation and metastatic competence *Biophys. J.* **88** 3689–98
[75] Wottawah F, Schinkinger S, Lincoln B, Ebert S, Müller K, Sauer F, Travis K and Guck J 2005 Characterizing single suspended cells by optorheology *Acta Biomater.* **1** 263–71
[76] Webb H K, Truong V K, Hasan J, Crawford R J and Ivanova E P 2011 Physico-mechanical characterisation of cells using atomic force microscopy—current research and methodologies *J. Microbiol. Methods* **86** 131–9
[77] Davidson L A, Koehl M A R, Keller R and Oster G F 1995 How do sea urchins invaginate? Using biomechanics to distinguish between mechanisms of primary invagination *Development* **121** 2005–18
[78] Lekka M, Laidler P, Gil D, Lekki J, Stachura Z and Hrynkiewicz A Z 1999 Elasticity of normal and cancerous human bladder cells studied by scanning force microscopy *Eur. Biophys. J.* **28** 312–6
[79] Takeichi M 1987 Cellular and molecular basis for tissue construction: role of cadherins in selective cell adhesion *Seikagaku* **59** 1–9
[80] van der Linden P J 1996 Cell adhesion, cell adhesion molecules and their functional role in the human endometrium *Early Pregnancy* **2** 5–14
[81] Indovina P, Ferrante A, Rainaldi G and Santini M T 2006 Hypoxia and ionizing radiation: changes in adhesive properties and cell adhesion molecule expression in mg-63 three-dimensional tumor spheroids *Cell Commun. Adhes.* **13** 185–98
[82] Benoit M, Gabriel D, Gerisch G and Gaub H E 2000 Discrete interactions in cell adhesion measured by single-molecule force spectroscopy *Nature Cell Biol.* **2** 313–7
[83] Chesla S E, Selvaraj P and Zhu C 1998 Measuring two-dimensional receptor-ligand binding kinetics by micropipette *Biophys. J.* **75** 1553–7
[84] Piper J W, Swerlick R A and Zhu C 1998 Determining force dependence of two-dimensional receptor-ligand binding affinity by centrifugation *Biophys. J.* **74** 492–513

[85] Saucedo L J and Edgar B A 2002 Why size matters: altering cell size *Curr. Opin. Genet. Dev.* **12** 565–71
[86] Vintermyr O K and Døskeland S O 1987 Cell cycle parameters of adult rat hepatocytes in a defined medium. A note on the timing of nucleolar DNA replication *J. Cell Physiol.* **132** 12–21
[87] Mahaffy R E, Shih C K, MacKintosh F C and Käs J 2000 Scanning probe-based frequency-dependent microrheology of polymer gels and biological cells *Phys. Rev. Lett.* **85** 880–3
[88] Alcaraz J, Buscemi L, Grabulosa M, Trepat X, Fabry B, Farre R and Navajas D 2003 Microrheology of human lung epithelial cells measured by atomic force *Biophys. J.* **84** 2071–9